Periodico di Mineralogia
ISSN: 0369-8963

Volume 94, No. 2, 2025

GEOLOGY, GEOCHEMISTRY AND FLUID INCLUSION STUDIES OF THE VEIN-TYPE FATHABAD CU±AU DEPOSIT, KHAF-KASHMAR-BARDASKAN METALLOGENIC BELT, NE OF IRAN

Hanieh Kiaee [1], Ahmad Kazemi-Mehrnia [1]*, Hamid Samari [1, 2], Peyman Afzal [3], Nazanin Zaheri-Abdevand [1], Hamed Ebrahimi Fard [4], Mohammad Ali Aliabadi[1]

[1] Department of Earth science, Mahallat Branch, Islamic Azad University, Mahallat, Iran
[2] Global Resource Engineering, Denever, USA
[3] Department of Petroleum and Mining Engineering, South Tehran Branch, Islamic Azad University, Tehran, Iran
[4] Department of Geochemistry, Faculty of Earth Sciences, Kharazmi University, Tehran, Iran

*e-mail: akmehrnia@yahoo.com

ABSTRACT

The Fathabad deposit is located in the village of Fathabad in the central district of Roshtkhar County, Razavi Khorasan Province, Iran. It is hosted by felsic to volcanic rocks including basaltic-trachyandesite, trachybasalt, trachyandesite, trachydacite and rhyolite in composition. The geochemistry of the Fathabad volcanics is consistent with high-K calc-alkaline to shoshonitic and metaluminous to peraluminous features, characterized by low to high SiO_2 (47-74.70 wt.%), Sr/Y (4.5-161) and $(La/Yb)_N$ (3.99 to 37.06); An enrichment of LILEs and LREEs and a depletion of REEs and HFSEs. Hydrothermal alteration has produced a zone of silicification, propylitic and Fe-oxide and hydroxide alteration associated with minor sericite-argillic alteration. Field and mineralogical studies indicate that mineralization has occurred in the form of hypogene and supergene. Microthermometric measurements of the primary LV fluid inclusions in quartz and calcite indicate that the ore-forming fluids belong to the $H_2O+NaCl+CaCl_2$ system with low to intermediate temperature (85 to 210°C) and salinity (12.30 to 23.83 wt.% $NaCl+CaCl_2$ equiv.) in quartz and a temperature of 135 to 208°C with a salinity between 17.33 and 23.05 wt.% $NaCl+CaCl_2$ equiv. in calcite. Mineralization is related to the mixing and cooling of magmatic and meteoric fluids. The $\delta^{34}S$ isotope values (-1.58 to -2.86‰) in the chalcopyrite minerals indicate the magmatic origin of the sulfur. Due to the structural control of mineralization and alteration, the moderate to low temperature and salinity of the ore fluid, and the petrogenesis of the volcanic rocks, the Fathabad Cu±Au deposit is similar to epithermal deposits.

Keywords: Fathabad Cu±Au deposit, geochemistry, fluid inclusion study, Khaf-Kashmar-Bardaskan metallogenic belt, epithermal deposits.

https://doi.org/10.5281/zenodo.15130089

INTRODUCTION

In recent decades, a new type of iron ore deposit called iron oxide-copper-gold (IOCG) deposit has been introduced by various researchers (e.g., Hitzman et al., 1992, 2000; Zhu, 2016). Iron oxide-apatite (IOA) (e.g., Kiruna type) and iron oxide-copper-gold (IOCG) (e.g., Olympic Dam) deposits are among the most important iron oxide-rich deposits in the world, with high economic importance as sources of Fe, Cu, Au, Ag, Bi, P, Co, Nb, U and REEs (e.g., Hitzman, 2000; Williams et al., 2005; Barton, 2014; Simon et al., 2018; Chen et al., 2019; Huang et al., 2019; Xing et al., 2019; Verdugo et al., 2020; Skirrow, 2022). Previous studies have also shown that IOA and IOCG deposits are genetically related to iron skarn deposits (e.g., Li et al., 2023). These deposits are associated with intense Na-Ca-K metasomatism. On the other hand, the formation of this type of deposit spans the Late Archean (Childress et al., 2016; DeMelo et al., 2017, 2019a, b) to Plio-Pleistocene (Naranjo et al., 2010; Moreto et al., 2015).

These deposits are associated with intermediate to mafic masses such as gabbro, diorite and calc-alkaline to alkaline granodiorite of I-type (oxidant or magnetitic) nature in continental margin extensional tectonic settings associated with subduction zones, intracontinental rifts or hotspots (e.g., Haynes, 2000; Hitzman, 2000; Sillitoe and Burrows, 2003; Barton and Johnson, 2004; Pollard, 2006; Dare et al., 2015; Westhues et al., 2016, 2017a, b). World-class IOCG and IOA deposits are predominantly Precambrian in origin and formed in intracratonic environments. Smaller Phanerozoic deposits are associated with convergent margin tectonic environments (e.g., Sillitoe, 2003; Williams et al., 2005; Mumin et al., 2007; Groves et al., 2010; Barton, 2014; Simon et al., 2018).

In IOCG deposits, the function of ore-forming fluids is intense and different alterations occur depending on the host rock type and depth of the formation. Sodic-calcic alteration is an important feature of these deposits (e.g., Groves et al., 2010; Corriveau et al., 2017; Hunger et al., 2018; Huang et al., 2019; Veloso et al., 2020; Skirrow, 2022; Leao-Santos et al., 2022). The vertical and uniform distribution of structural controllers in these systems reinforces the hypothesis that these two types of mineralization are part of a common mineral system (e.g., Day et al., 2016). In economic terms, the most important areas of IOCG-type iron mineralization, in order of age, are the Central Andes (Cu+Fe; Mesozoic; Sillitoe, 2003), the Lower Yangtze (Fe+Cu; Mesozoic; Yang et al., 2011), the Southern Urals (Fe; Paleozoic; Hawkins et al, 2010), South Australia (Cu-U-Au; Mesoproterozoic; Hayward and Skirrow, 2010; Skirrow and Davidson, 2007), North Central Australia (Cu+Au; Paleo to Mesoproterozoic; Williams, 1998; Williams and Pollard, 2001), the North Baltic (Fe+Cu; Paleoproterozoic; Billstrom et al., 2011; Frietsch et al., 1997) and the Carajas (Cu+Au; Late Archean; Xavier et al., 2011).

Iron oxide-copper-gold (IOCG) deposits were first introduced in Iran by Karimpour et al. (2003, 2005). Iron oxide-apatite (IOA) and iron oxide-copper-gold (IOCG) deposits in Iran were formed in tectonomagmatic evolution related to Early Cambrian intracratonic magmatism in central Iran and Cenozoic subduction-related magmatism in the Alborz Magmatic Arc (AMA) (Nabatian et al., 2015). IOCG-type iron deposits containing significant amounts of Au, Cu, U, Bi and Co have been recorded in the Bafq metallogenic belt in central Iran (e.g., Jalalabad Zarand; Mehrabi et al., 2019).

The Fathabad Cu±Au deposit is located in the Khorasan Razavi province, in Roshtkhar County. Structurally, it is located in the Central Iran Structural Zone (Figure 1), approximately 35 km southeast of Torbat-e-Heydariyeh, in the Khaf-Kashmar-Bardaskan Metallogenic Belt (KKBMB) of northeastern Iran along the east-west trending internal regional fault (Figure 1). The KKBMB in north-eastern Iran is one of the major metallogenic provinces with high potential for the exploration of various porphyry, vein, skarn and IOCG copper, gold, silver and iron-bearing deposits hosted by volcanic-pyroclastic rocks. Numerous small to medium-sized precious and base metal deposits and occurrences have been discovered and reported in the KKBMB, most of which are hosted by Eocene volcanic and volcaniclastic rocks.

The province is host to numerous mineral deposits, such as the Sangan iron skarn deposit (e.g., Malekzadeh Shafaroudi et al., 2013, 2016; Golmohammadi et al., 2014, 2015; Mazhari et al., 2017; Sepidbar et al, 2017; Mehrabi et al., 2021; Ghasemi Siani et al., 2022), the Tanourjeh porphyry copper-gold deposit (Karimpour and Malekzadeh Shafaroudi, 2007), the Kuh-e-Zar gold-copper-specularite deposit (Karimpour et al., 2017), Zaveh vein copper deposit (Berouzi Niat et al., 2019), Shahrak gold-copper-specularite-magnetite deposit (Yousefi-Sourani et al., 2008), Namagh vein-type deposit of iron oxide-copper (IOCG) mineralization (e.g., Taghadosi et al., 2018), Roshtkhar IOCG iron deposit (Biabangard et al., 2017), Rashidi epithermal vein-type copper deposit (e.g., Javidi Moghaddam et al., 2020), Sharifabad Bardaskan manto-type copper deposit (e.g., Ebrahimi et al., 2020). This belt contains large iron deposits, and significant copper and gold deposits have also been discovered or exploited. The Fathabad Cu±Au deposit has an estimated mineral reserve of approximately 600,000 tons at 0.42% Cu and 0.96 ppm Au. In general, mineralization has occurred on fault boundaries which, given the iron and copper mineralization in the region, are considered to be of IOCG type and the role of hydrothermal fluids in the formation of the major regional alterations has been recognized (Yusefi Sourani, 2006). Although the geology suggests an epithermal deposit, the mineralogy of the ore, the characteristics and nature of the ore-forming fluid and the origin and tectonic setting of the host rocks remain uncertain. In this paper we investigate the geological and geochemical characteristics of volcanic rocks and quartz and calcite vein intercalations of the Cu±Au deposit at Fathabad. The aim of this research is to investigate the occurrence of the Cu±Au vein deposit at Fathabad-Roshtkhar based on geological, geochemical and fluid intercalation studies.

REGIONAL GEOLOGY

The geology, tectonics and location of minerals in Iran have been greatly influenced by the evolution and changes of the Tethys Ocean. Tectonic events around the Iranian plate are related to the process of Gondwana separation and collision with the Arabian plate from the southwestern side of Iran. This important process affected the Iranian plate and adjacent plates such as Africa, India, Arabia and Eurasia during the Mesozoic to Tertiary (Alavi, 2004; Esmaeili, 2019). The Iranian Tethys is located in the central part of the Alpine-Himalayan orogenic belt, which is the result of the closure of the Neo-Tethys between Eurasia and Gondwana (e.g., Alavi, 1991; Stampfli and Borel, 2002; Metcalfe, 2013; Wu et al., 2015; Zhai et al., 2016; Li et al., 2018).

As a result of the development of the Neo-Tethys Ocean, including its opening, subduction and closure, and subsequent events, a number of magmatic processes occurred in Iran, one of the most important of which occurred in the Late Cretaceous (Kazemi et al., 2019). The Iranian arcs were formed during the northward subduction of the Neo-Tethys oceanic lithosphere and its extensive extension during the Upper Cretaceous and Paleogene. This expansion stops at the time of the collision with the Arabian plate and the beginning of the Neogene (Spidbar et al., 2019). The Central Iranian Microplate is a north-south trending structural unit consisting of three blocks: Lut, Tabas and Yazd (Khazaei et al., 2018). The Lut Block, as one of the major structural zones of Iran, was part of Gondwana until the emergence of the Neotethys in the Permian (e.g., Crawford, 1972; Stampfli and Borel, 2002; Ramezani and Tacker, 2003; Golonka, 2004; Rashidi et al., 2019, 2021, 2022; Javidi Moghaddam et al., 2021; Arjmandzadeh et al., 2022). Most studies of the Lut Block have emphasized the issue of subduction and considered the magmatism and deposits of eastern Iran to be related to it (e.g., Berberian and King, 1981; Camp and Griffis, 1982). Others have rejected subduction and attributed magmatism and mineralization formation to the presence of tensile conditions (e.g., Saadat et al., 2016; Khatib et al., 2016; Spidbar et al., 2018; Javidi Moghaddam et al., 2019, 2021; Arjmandzadeh et al., 2022; Raeisi et al., 2023; Mazhari et al., 2023). The subduction theory proposes the existence of a complete orogenic cycle, including rifting, formation of a small ocean between the Lut and Afghan blocks, subduction of oceanic crust, ocean closure and collision of the Lut and Afghan blocks.

Khorasan province is located in a part of the central Iranian subcontinent that is divided from east to west by the Dorouneh-Kalmard and Nehbandan faults into the Tabas, Yazd and Lut blocks (Aghanabati, 2013) (Figure 1). The Khaf-Kashmar-Bardaskan volcano-plutonic belt forms an important part of the central Iranian subcontinent, more than 350 km long and 15-80 km wide with an east-west to northwest-southeast trend, located between the Neo-Tethys fault and the back of the Sabzevar-Alborz magmatic arc (Alaminia et al., 2013) (Figure 2). Research and exploration studies on magmatism and mineralization of eastern and northeastern Iran in the Khaf-Kashmar-Bardaskan belt indicate several magmatic events and intrusions of granitoid bodies and tuffs and acidic, intermediate to mafic volcanic lavas of Paleocene to Eocene age related to the subduction of the convergent margin of the oceanic-continental crust of Andean type in this belt (e.g., Malekzadeh-Shafaroudi et al., 2013; Alaminia et al., 2013; Asiabanha and Foden, 2012; Golmohammadi et al., 2015).

The Roshtkhar area is located in the Khaf-Kashmar-Bardaskan volcanic-plutonic belt in northeastern Iran, along the east-west trending Dorouneh fault, southeast of the Lut block. There are several outcrops of volcanic rocks intruded into Cenozoic intrusive rocks as dikes (Alizadeh et al., 2017). It is generally accepted that subduction of the Sabzevar oceanic crust (as a Cretaceous back-arc basin) beneath the Turan block led to magmatism along the Sabzevar region in the Late Cretaceous-Early Eocene (e.g., Alaminia et al., 2013; Jamshidi et al., 2015; Maghfouri et al., 2016).

The Fathabad Cu±Au deposit, located on the eastern margin of the KKBMB (Figure 2), is part of the Central Iranian Microcontinental Zone. The KKBMB is a W-E to NW-SE trending Cenozoic volcanic-plutonic belt, 350 km long and 15-80 km wide, located south of the major Dorouneh fault, which separates the KKBMB from the southern Lut block (Figure 2). As a result of the dextral and sinistral movements of the Dorouneh fault, the Sabzevar block has formed to the north and the Lut block to the south of the Dorouneh fault. The structural features of the KKBMB, such as faults and folds, are aligned with the E-W direction of the Dorouneh fault (Figure 2). The KKBMB is largely composed of Cenozoic acidic, intermediate and mafic volcanic rocks which are intruded by granitic to dioritic intrusions. Within the KKBMB we observe intermediate to acidic tuffs, lavas and intrusions exposed by a combination of monzonite, granodiorite and granite. According to recent studies, the KKBMB is considered to be a convergent margin of Andean-type subduction of oceanic-continental crust during the Paleogene (Golmohammadi et al., 2015).

The Fathabad deposit is located north-east of the Roshtkhar 1:100,000 geological map (Ternet et al., 1980) and south of the Dolatabad 1:100,000 geological map (Khasraghi et al., 1996) (Figure 3). The Fathabad deposit is considered part of the Sabzevar structural subzone in terms of structural subzones. The Sabzevar-Torbat-e-Jam subzone includes limited areas between the Miami-Bedrock Fault and the Dorouneh Fault, which trends approximately east-west from Sabzevar to the Afghanistan border. In this subzone, Paleozoic and Mesozoic rocks have limited outcrops. Lower Triassic rock units are not observed in the area, but Middle Triassic deposits are outcropped in the northeast of the area. These deposits begin with diabase to olivine diabase and continue with thick-bedded, ridge-forming yellow to reddish-brown dolomites equivalent to the Shotori Dolomites of central Iran. The Upper Triassic deposits consist of shales and sandstones interbedded with fossiliferous limestones, which are differentiated by lithology and stratigraphic position. Jurassic deposits include the Shemshak Formation and quartzite conglomerate. The Shemshak Formation sediments are mainly exposed in the south-west and south-east of the region. The deposits of the Shemshak Formation have been altered to albite-epidote hornfels facies due to their contact to granodiorite bodies. Quartzite conglomerate deposits are exposed in the southwest of the area with a northwest-southeast trend. Early Cretaceous sediments in the area include conglomerate units, sandstone, orbitolinid limestone, shale and andesite (Figure 3).

The Late Cretaceous sediments of the region include conglomerate units, sandstone, glauconite limestone, limestone-marl, limestone, shale and sandstone-marl. In the south of the study area, the Eocene sediments are outcrops of conglomerate units which are angularly unconformity with Paleocene, Cretaceous and older deposits and are progressively and uniformly overlain by sandstone and, in parts of the area, by volcanic rocks. In the southern part of the area, a series of volcanic rocks including porphyry andesite, andesite to pyroxene andesite, crystalline tuff, lithic tuff and others are exposed with a northwest-southeast trend. After the deposition of the Eocene-Oligocene sediments mentioned above and after a period of sedimentation, a series of clastic sediments (conglomerate, sandstone, shale and marl) remained on top of the Eocene and older sediments. These sediments appear to be equivalent to the Oligocene sediments (Figure 3).

GEOLOGY OF THE FATHABAD DEPOSIT

The stratigraphic units outcropping in the Fathabad deposit include Eocene volcanic and volcanic-sedimentary units and Miocene granitic intrusive units (Figure 4). The Eocene conglomerate (Ec) consists of grains 2 mm to 35 cm thick, sometimes even larger than the Paleocene conglomerate fragments and Cretaceous limestones. This conglomerate is unconformably deposited on sandstones of the Es unit on top of Paleocene and Cretaceous deposits, and is covered in parts of the area by volcanic rocks of the Ea unit. The volcanic rocks of unit (Ea) are porphyritic andesite, andesite to pyroxene andesite, crystalline tuff and lithic tuff. The volcanic rocks of subunit (Er) are andesite, rhyolite and lithic tuff, corresponding to the volcanic rocks of unit (Ea). This unit is discontinuously covered by Quaternary alluvial fans and alluvium (Qt). The Eocene volcanic units in this area are divided into two parts (Figure 5a). The first part consists of a dark grey, mega porphyritic andesite unit with sandy tuff interbeds exposed in the eastern and northern center (Figure 5b). The second part consists of light grey mega porphyritic andesite (Figure 5c), porphyritic quartz intruded in agglomerate and breccia volcanics. The second part is exposed in the west and center of the study area and has been heavily sheared due to its proximity to the Dorouneh fault. It has undergone extensive sericitic, argillic and propylitic alteration (Figure 5c). The agglomerate unit consists of volcanic fragments of various sizes that are stratified due to poor sorting and rounding (Figure 5d). Granitic to granodiorite (gd) intrusive unit rocks have intruded the Eocene altered-mineralized rock units. These granular, medium-to-coarse-grained rocks consist of plagioclase, potassium feldspar, quartz, and biotite (Figure 6f). Eroded crystals of the (gd) unit were found within the Eocene conglomerate (Ec), which was covered by Quaternary sediments such as alluvial terraces and fluvial deposits (Kholghi-Khasraghi, 1990). This intrusive covered sediments from the Miocene to the Quaternary, making it most likely Miocene in age. However, Golmohammadi et al. (2015) suggested that it is a calc-alkaline, subduction-related I-type granitoid belonging to the Middle Eocene (39.1±0.6 to 38.3±0.5 Ma; zircon U-Pb dating).

The presence of alteration and mineralization in the form of rare veinlets in the granitic intrusive rocks (Figure 6e) to the south-east of the Fathabad area may indicate that it acts as a heat engine, causing the establishment of hydrothermal fluid cycles in the volcanic rocks. In addition, the NE-SW trending minor -faults in the region also served as a pathway for hydrothermal-magmatic fluids associated with the granite intrusion, resulting in the strong alteration and mineralization within these faults. Since the intrusive granite unit shows mineralization and alteration, it is considered to be the main source of mineralization in the district (Biabangard et al., 2017).

STRUCTURAL GEOLOGY

The study area has a complicated tectonic structure due to the activity of various faults and fractures. The presence of the Dorouneh strike-slip fault (W-E) with a dip of N40W, which forms a large shear and fault zone consisting of several NE-SW-trending minor faults, is the main structural geological feature in the northwest of the Fathabad district (Figure 1b, c). The NE-SW trending minor faults have severely fractured the exposed Eocene volcanic units in this area. In general, there are two generally trending fractures and faults; the first set consists of NW-SE faults cutting through the volcanic rocks with no correlation between alteration and mineralization (Javadi et al., 2013). Most of the mineralized quartz veins are parallel to right-angle, short, discontinuous NE-SW faults, indicating that they played an important role in controlling the deposition of mineralization. (Figures 6c, d, 8a, b). The ore zone in the Fathabad area is attributed to NE-SW minor faults of the Dorouneh fault.

ALTERATION FEATURES

Based on field and microscopic studies and XRD analyzes, the main alteration types in the study area include silicification, argillic, phyllic (or sericitic), carbonatization, iron oxide, hydroxide and propylitic alteration. Propylitic alteration is characterized by a wider extent compared to other alteration zones observed along the margins of mineral veins (Figure 6b). Close to the veins, silicic and sericitic alteration dominates. With distance, the intensity of argillic and propylitic alteration progressively increases (Figures 6b, 8b). Field observations and petrographic analysis confirm the presence of silicic alteration in the form of veinlets and veinlets. This alteration style is commonly associated with mineralization. Microscopic examination also reveals disseminated fine-grained quartz crystals within the volcanic matrix, indicative of silicification, and coarse-grained calcite filling the space between the older quartz crystals (Figure 7a). The abundance of quartz can be attributed to increased permeability induced by tectonic forces. This is further evidenced by the variety of quartz textures such as comb, blade, sheard, cavity filling and radial which are characteristic of epithermal deposits (Guilbert and Park, 1991). Quartz, calcite, montmorillonite-chlorite, sericite, muscovite, illite, kaolinite and albite are the main alteration minerals identified in thin sections and by XRD analysis.

Along the NE-SW trending fault, propylitic alteration has affected the volcanic rocks extensively and irregularly (Figure 6d, 8a). Disseminated copper mineralization occurred in association with propylitic alteration in the mega porphyritic andesite (bornite, chalcopyrite, chalcocite, covellite, goethite, hematite, limonite, magnetite, malachite, pyrite) (Figures 6c, d, 8b). Propylitic alteration is often accompanied by argillic alteration (Figure 6a, b) and sometimes occurs as narrow bands along the margins of mineralized quartz veins (Figure 6c). The ubiquitous alteration minerals of propylitic alteration, which produces greenish colored rocks, consist of epidote and chlorite with variable amounts of calcite, magnetite, with minor amounts of sericite and quartz. Typically, Fe-Mg silicates and plagioclase (Figure 4c, d) are altered to an assemblage of chlorite, epidote, Fe oxides and calcite. Iron oxides and hydroxides are often found at the margins and in microfractures of primary minerals (Figure 5c, d).

Argillic alteration is often accompanied by propylitic alteration and secondary iron oxides and hydroxides (Figure 6b). Based on the XRD results (Appendix Table 1), illite, kaolinite and montmorillonite have been identified from the argillic alteration. Argillic alteration is characterized by intense decomposition of potassium feldspar and plagioclase into clay minerals (Figure 6b). Iron oxides and hydroxides are common along fractures and fractures of phenocrysts. The

https://doi.org/10.5281/zenodo.15130089

predominant alteration associated with mineralization is silicification, usually in the form of quartz veinlets along NE-SW trending fracture zones (Figures 6c, d, 8a). Quartz occurs irregularly throughout the rocks and in veins with sericite margins (Figure 7b). Carbonate alteration was spatially heterogeneous and occurred in the form of veins. (Figure 7a). Sericite alteration is commonly associated with silicification and ore-bearing veins (Figure 8f). The XRD results of the sericite alteration show that the clay mineral is mainly illite and chlorite. Plagioclase is consistently affected by strong sericitization (Figure 7c, d). Hematite, limonite and goethite are common in the area and are yellow to orange-yellow and red-brown in color (Figure 6b).

MINERALIZATION

Ore mineralization and sedimentation within the Fathabad exploration distinct has occurred in two distinct stages, influenced by tectonic conditions. The first stage exhibits a symmetrical pattern characterized by a sparse distribution of valuable elements within the intrusive body. During this stage, mineralization occurs as disseminated concentrations of pyrite within the intrusive body. This is followed by the second stage, which is associated with the fault systems that follow a northeast-southwest trend. Alteration and traces of chalcopyrite and gold mineralization have been observed along these primary faults. These sediments are hosted in silicic veins permeated by iron and manganese oxides hosted in volcanic and conglomerate rock units (Kazemi, 2016).

Mineralization at the Fathabad deposit is characterized by disseminated open space fillings and veinlets along faults and fractures of Eocene porphyritic andesites (Figure 8b) and agglomerate units (Figure 8c). The quartz veins vary in length from less than 50 to 200 meters and can be traced with discontinuous outcrops (Figure 6d). Occasionally calcite crystals are observed along with quartz veins (Figure 8c). Mineralogical studies have generally shown that the mineralization can be divided into hypogene and supergene mineralization (Figure 9). Hypogene minerals include pyrite, chalcopyrite and magnetite. Supergene minerals include chalcocite, covellite, malachite, hematite, goethite and limonite. Gangue minerals include quartz, epidote, chlorite and albite. The crystals of chalcopyrite have changed from the edge to chalcocite and bornite (Figure 8f) and are altered to Fe oxide hydroxides (goethite, hematite and limonite) (Figure 8f). Covellite has often replaced chalcopyrite (Figure 5e; Figure 7a). Pyrite occurs as euhedral and/or subhedral crystals (Figure 8e), which are disseminated and as open spaces filling. Euhedral to subhedral magnetite (Figure 10b) is altered to hematite (Figure 10c, d). Malachite, goethite, hematite and limonite (Figures 8b, d, 10b, c) are the most common secondary minerals resulting from the supergene alteration of magnetite and chalcopyrite minerals (Figure 9).

EXPERIMENTAL

SAMPLE DESCRIPTION

For the purposes of this study, 57 drill core and outcrop samples were collected from volcanic host rocks. Approximately 21 host rock samples were of different lithologies and 12 samples were collected from mineralized veins. Approximately 8 double polished sections were prepared from quartz and calcite veins hosted in volcanic rocks. Approximately 12 samples were selected for whole rock chemical analysis, focusing on the least altered rocks.

GEOCHEMISTRY

The major and trace element chemical compositions of about 12 volcanic rock samples (Appendix Table 2) were measured by wavelength dispersive X-ray fluorescence spectrometry (XRF) and an inductively coupled plasma mass spectrometer (ICP-MS) at the Iranian Mineral Processing Research Center (IMPRC) in Karaj, Alborz Province, Iran. These techniques are widely used in geological analysis for the determination of major and trace elements. The analysis focused on major oxides and the determination of minor, rare and rare earth elements. In ICP-MS analysis, element dissolution is achieved by the multi-acid digestion method, together with the use of microwave digestion. The resulting solution is then analyzed using an ICP-MS instrument. The analysis of major oxides by X-ray fluorescence is based on the behavior of atoms as they interact with X-rays. In this method, samples are ground to a size finer than 200 mesh and then analyzed by X-ray fluorescence (XRF) in the laboratory. The accuracy of this analysis is within 0.01 per cent by weight. When materials are exposed to high energy, short wavelength radiation (such as X-rays), they can be ionized. The representative whole rock analyses of the Fathabad volcanic rocks are presented in (Appendix Table 2).

In addition, to identify the unknown mineral phases, eight samples were subjected to X-ray diffraction (XRD) analysis using a Philips Pro Xpert instrument under Co Kα conditions (1/789010A) at the Iran Mineral Processing Research Centre (IMPRC) in Karaj, Alborz Province, Iran. X-ray diffraction (XRD) data are presented in (Appendix Table 1).

MICROTHERMOMETRY

Based on petrographic studies of primary fluids associated with quartz and calcite, approximately 8 double polished wafers (each 100 μm thick) containing suitable fluid inclusions (>4 μm in size) were carefully analyzed. These were selected for microthermometric measurements. The microthermometric study was carried out at the Fluid Inclusions Laboratory, Iranian Mineral Processing Research Center (IMPRC), Alborz Province, Iran, using a Linkam THMS-600 heating/freezing stage with a temperature range of -196°C to +600°C. The instrument has been previously calibrated at low temperature with n-hexane (-94.3°C) and at high temperature (+414°C) with cesium nitrate. The estimated accuracy of the measurements is ±0.2°C for temperatures below 31°C and ±1°C for the interval 31-300°C. The results of the microthermometry study are summarized in (Appendix Table 3).

RESULTS

WHOLE ROCK GEOCHEMISTRY

The samples selected for geochemical analysis underwent a thorough macroscopic and microscopic examination. Ultimately, only samples with minimal alteration were selected for analysis. Despite the good quality of the geochemical analyses, the wide range of results observed in the geochemical diagrams can be attributed to the influence of hydrothermal fluids in the district. The volcanic rocks analyzed in this study show a wide range of SiO_2 (47-73.6 wt.%), high Al_2O_3 (13.2-19.2 wt.%), Na_2O (3.27-4.12 wt.%), low to high K_2O (0.67-5.87 wt.%), CaO (0.88-9.37 wt.%), Sr (45-704 ppm) and TiO_2 (0.41-1.23 wt.%), CaO (0.88-9.37 wt.%), Sr (45-704 ppm) and TiO_2 (0.41-1.23 wt.%), Fe_2O_3 (1.5-9.69 wt.%), MgO (0.2-7.31 wt.%), Ni (5.7-84.9 ppm), Cr (62-156 ppm) contents (Appendix Table 2).

The volcanic rocks are shown in the Na_2O+K_2O vs. SiO_2 diagram Le Maitre (2002), within trachybasalt, basaltic trachyandesite, trachyandesite/trachyte and rhyolite fields (Figure 11a). Most of the volcanic rocks are peraluminous and some are metaluminous (Figure 11c) and plot in the calc-alkalic to shoshonitic domains on a K_2O vs. SiO_2 diagram (Peccerillo and Taylor, 1976; Figure 11b). Major elements such as Fe_2O_3, MgO and Al_2O_3 are negatively correlated with increasing SiO_2 content (Figure 12a, c, e). In trachybasalt and basaltic-trachyandesite samples, P_2O_5, Sr and Co increase with SiO_2 (Figure 12f, g, h), whereas in trachydacite and rhyolite samples they decrease with increasing SiO_2 (Figure 12f, g, h). Primitive mantle normalized REE patterns for the rocks studied (Sun and McDonough, 1989; Figure 13a), show moderate to high LREE enrichment ($(La/Yb)_N$=3.99-37. 6) relative to HREE, with slightly negative Eu anomalies for all samples analyzed (Eu/Eu* of 0.19-1.06), except one basaltic trachyandesite sample with positive Eu anomaly (Eu/Eu* of 1.37) (Appendix Table 2). Eu/Eu* ratios (0.19-1.37; ~0.80) show a rough negative correlation with SiO_2 content (Figure 13a). On the primitive mantle normalized trace element distribution diagram (Sun and McDonough, 1989; Figure 13b), these rocks show enrichment in large ion incompatible elements (LILE) and depletion in high field strength elements (HFSE). They are also characterized by negative anomalies in Rb, Th, Ta, La, Ce, Pr, P, Zr, Hf, Eu and Y, and positive anomalies in Ba, U, K_2O, Pb, Sr, Nd, Sm, Gd and Dy. The data fall in and near the Adakite field on the (Sr/Y) vs. Y and (La_N/Yb_N) versus Yb_N discrimination plots (Figure 16a, b), with Sr/Y and $(La/Yb)_N$ ratios ranging from 4.5 to 161 and 3.99 to 37.6, respectively (Appendix Table 2).

FLUID INCLUSION PETROGRAPHY

A total of 131 (LH_2O+vapour) primary fluid inclusions were analyzed in 6 double polished sections (100 μm thickness), including quartz and calcite crystals associated with sulfides from the Fathabad deposit, and their microthermometric results are presented in (Appendix Table 3). Based on the phase compositions at room temperature, liquid-rich two-phase (LH_2O+vapour) (quartz and calcite) inclusions (Figure 14a, b) and mono-phase (L-type) FIs (Figure 14b) have been identified. In all mono-phase (L-type) FIs there is a pure liquid in the cavity of the inclusion and there is no vapor phase. The mono-phase FIs usually have a negative crystal shape and irregular shapes that are distributed in the quartz and calcite crystal planes. They are small, most being 4-12 μm in size (Figure 14b). Primary two-phase (LH_2O+vapor) FIs have a filling ratio of typically 0.80 vol% liquid and have variable shapes (negative, oval, round, elliptical and irregular). They are typically 4 to 35 μm in size (Figure 14a, b; Appendix Table 3). Two phase L+V FIs were mainly observed as either negative crystals, spherical, elliptical or irregular in shape. Cooling experiments did not

https://doi.org/10.5281/zenodo.15130089

reveal liquid CO_2 or clathrate formation, suggesting that none of the inclusions contained significant amounts of CO_2. In addition, there was no evidence of fluid boiling in the Fathabad samples. The temperatures of homogenization (Th), eutectic phase change (Te) and final melting of ice (Tm_{ice}) were measured for each inclusion. Salinities of liquid-rich FIs were calculated using the final ice melting temperature (Tm_{ice}) and the formula of Bodnar (1993). Densities and pressures were calculated using Flincor software from microthermometer data from Brown (1989).

FLUID INCLUSION MICROTHERMOMETRY

In the Mineralogy Laboratory at the Materials Processing Research Centre, we have carried out precise temperature measurements on minerals using advanced equipment. Key components of our facility include:

THMS600 stage: This stage allows controlled heating and freezing experiments, ensuring accurate data collection.

Linkam model: Integrated with the THMS600, this model provides precise temperature control during experiments.

ZEISS Axioplan2 microscope: Equipped with imaging capabilities, this microscope enhances observation during temperature studies. The thermal range covered by our instrument is from -196°C to +600°C.

The results of our analysis are summarized in (Appendix Table 3). Microthermometric data obtained from fluid inclusions show eutectic melting temperatures (Te) below -41°C. These data are consistent with a hydrothermal fluid system composed primarily of H_2O-NaCl-$CaCl_2$ (and possibly KCl) (Shepherd et al., 1985). The two-phase (L+V) FIs give final ice melt temperatures (Tm (ice)) of -8.4 to -24.7°C in quartz (Appendix Table 3); and -14 to -21 ◦C in calcite (Appendix Table 3). The salinity of L+V inclusions ranges from 12.30 to 23.83 (with a mean of 21) wt.% NaCl+$CaCl_2$ equivalent in quartz and from 17.33 to 23.05 (with a mean of 19) wt.% NaCl+$CaCl_2$ equivalent in calcite (Figure 14 a). Two-phase (LV) FIs in quartz and calcite were homogenized to liquid inclusions at temperatures varying from 85 to 210 °C (with a mean of 150 °C) and 135 to 208 °C (with a mean of 160 °C), respectively (Appendix Table 3; Figures 19 a, b, 15 a, b). The calculated densities for LV FIs vary from 0.99 to 1.161 g/cm^3 (with a mean of 1.075 g/cm^3) in quartz (Appendix Table 3); and from 1.03 to 1.1 g/cm^3 (with a mean of 1.058 g/cm^3) in calcite (Appendix Table 3).

SULFUR ISOTOPE

For this study, 2 quartz vein samples identified as BHFA-B12 and BHFA-B35 were selected for sulfur isotope analysis of chalcopyrite. These samples are characterized by the composition of quartz, pyrite, chalcopyrite and chalcocite with silica-sericite alteration (Appendix Table 5). The source of sulfur in the ore-forming fluid was investigated by analyzing sulfur isotope values (expressed as $\delta^{34}S$) for 2 chalcopyrite samples extracted from mineralized quartz veins. These measurements were carried out specifically on the fluid associated with the above samples, as detailed in (Appendix Table 5). Notably, the $\delta^{34}S$ values for both chalcopyrite samples show a limited range, ranging from -1.58 to -2.86.

DISCUSSION

MAGMA SOURCE AND PETROGENESIS OF VOLCANIC ROCKS

The wide range of SiO_2 contents (47-74 wt.%) (Appendix Table 2) of the volcanic rocks indicates that the primary magma was either formed by partial melting of the mantle or underwent a low degree of evolution. Furthermore, the Cr (62-156 ppm) and Ni (5.7-85 ppm) contents of the studied volcanic rocks (Appendix Table 2) are much lower than those of primitive arc magmas (Cr = 364 ppm, Ni = 168 ppm) (Gudnason et al., 2012). The Fathabad volcanic rocks belong to the high-K calc-alkaline and shoshonitic series in a SiO_2 vs. K_2O diagram (Figure 11b). Most of the volcanic rocks are peraluminous and some are metaluminous (Figure 11c), as would be expected from their formation in subduction-related magmatic arc environments (Castro et al., 2013). Shoshonitic and high-K volcanic rocks are formed by partial melting of phlogopite. Phlogopite is formed by metasomatic minerals in the upper mantle from subducted oceanic crust (Bonin, 2004). The negatively correlated SiO_2 content with Fe_2O_3, MgO, P_2O_5 and Al_2O_3 of the Fathabad volcanic rocks (Figure 12a, b, d, e) can be interpreted by fractionation of magnetite, hornblende, plagioclase and biotite minerals (Li and Jiang, 2014). Plagioclase fractionation is responsible for the decrease in Al_2O_3 content with increasing SiO_2 content, which is also confirmed by decreasing Eu/Eu* ratios and Sr contents (Figure 12g, h).

Furthermore, the decrease in Al_2O_3 content suggests that plagioclase crystallization is important during magma differentiation. Decreasing P_2O_5 content with increasing SiO_2 reflects apatite fractionation (Figure 12e) (observed in XRF patterns). The Fathabad volcanic rocks show similar REE and trace element patterns (Figure 12a, b) to typical subduction arc volcanic rocks, suggesting a subduction affinity, that they originated from a common magma chamber and probably underwent similar fractionation pathways. According to the REE and trace element patterns normalized to the primitive mantle (Sun and McDonough, 1989) (Figure 13a), all rocks are characterized by LREE and LILE enrichment relative to HREE and HFSE and a negative Eu anomaly. High LREE/HREE and LILE /HFSE contents (Figure 12a) indicate that subduction played a dominant role in their petrogenesis (Walker and Mastalerz, 2004). Furthermore, the depletion of Rb relative to Ba in the primitive mantle normalized trace element distribution diagram (Figure 13b) and the relatively high Ba/Th ratios (>118) suggest the absence of residual amphibole in the source region. The Sr enrichment (Figure 13b) suggests that plagioclase is unstable at the partial melt pressures and temperatures at the magma source. Therefore, the positive Sr anomaly exhibited by almost all samples (Figure 13b) is probably not due to plagioclase accumulation. This confirms that no residual plagioclase was present during the melting process (Defant and Drummond, 1990).

Furthermore, the apparently negative or negligible Eu anomaly (Eu/Eu_N^* =0.19-1.37) suggests that early fractional crystallization of plagioclase can be ignored. The Fathabad volcanics exhibit geochemical characteristics similar to those of the adakites (Figure 16a, b), with high Sr (704-45 ppm; mean ~288 ppm), Sr/Y (704-45 ppm; ~288 ppm), La/Yb (37. 6-4 ppm; ~18), $(Ce/Yb)_N$ (31.5-4.8 ppm; ~15.2; and low Y (14.8-3 ppm; ~8.5 ppm), Yb (0.93-0.2 ppm; ~0.61 ppm), and

https://doi.org/10.5281/zenodo.15130089

Eu/Eu_N^* =0.19-1.37 (~0.80) (Appendix Table 2). The representation of the sample studied in the La/Yb vs. La diagram (Figure 17a) illustrates that partial melting was the most important genetic process. The $(La/Yb)_N$ ratios of the Fathabad volcanics range from 3.99 to 37.6 (average=18.6), suggesting that they were formed by partial melting of a variable residual garnet source.

According to the LREE enrichment and HFSE depletion (Figure 13a, b) and the Sm/Yb-La/Sm system melt modelling results (Figure 17b), it is confirmed that the parental melts of the Fathabad volcanics were derived by varying degrees of partial melting of a garnet-bearing lherzolite (garnet>spinel) from subduction-related metasomatized sub-arc mantle by slab-derived fluids (Luo et al., 2022). Melts from the garnet stability region have a Dy/Yb > 2.5, whereas a spinel-bearing source has a Dy/Yb< 1.5 (Yang et al., 2012). The Fathabad volcanics have Dy/Yb ratios ranging from 2.6 to 4.8 (Appendix Table 2), indicating that the mantle component is probably derived from the garnet lherzolite stability field. The residual garnet source can significantly increase both the $(La/Yb)_N$ and $(Dy/Yb)_N$ ratios of the magma. The positively correlated high $(Dy/Yb)_N$ and $(La/Yb)_N$ ratios (Figure 17c) suggest that garnet plays a dominant role in the REE fractionation during partial melting of the Fathabad samples.

The physicochemical information of the parent magmas, which in turn provides information on the metallogenic potential, can be inferred from the geochemical properties of the volcanic rocks formed in a comagmatic system (Richards, 2003). The strong to weak negative Eu anomaly and high Sr/Y ratio of the Fathabad volcanic samples indicate high water content and/or high oxygen fugacity of the parent magma (Ballard et al., 2002). Therefore, the high whole-rock Sr/Y ratio of the study samples (Sr/Y=4.53-161, mostly >20; Appendix Table 2) suggests the segregation of amphibole from a water-rich magma (Richards, 2011). Furthermore, Fe_2O_3 is positively correlated with MgO content (Figure 12i) for the trachyandesite and basaltic trachyandesite samples, indicating early separation of magnetite from the oxidized magma. The chalcophile elements (copper and gold) are more controlled by sulfides than melts under conditions of high oxygen fugacity (Sun et al., 2012). Extraction and dissolution of volatiles from oxidized and water-rich magma results in soluble metal-rich complexes. The high water content and oxygen volatility of the source magma may favor mineralization.

The Fathabad samples have negative Th and Ta and positive Pb anomalies (Figure 13b), indicating subduction and/or crustal contamination (Pearce, 1983). The high-K calc-alkaline to shoshonitic nature of these rocks (Figure 11b) and their characterization based on Th/Ta vs. Yb diagram (Gorton and Shandl, 2000) (Figure 18a) and Th/Nb vs. La/Yb diagram (Hollocher et al., 2012) (Fig. 18b), clearly support intra-plate and active continental margin and alkaline to oceanic island environment (Figure 18 a, b). On the Rb and Y+Nb discrimination diagram (Pearce, 1983) (Figure 18c), the volcanic rock samples show affinities to volcanic arc granites (VAGs), in an extensional environment (Figure 18c). High fractional crystallization in shallow extensional environments can result in variable compositions ranging from basaltic to rhyolitic in arc magmas similar to those in the Fathabad district. The volcanic rocks of the Fathabad deposit are mainly hosted near calc-alkaline to shoshonitic basalts (CAB) and within plate basalts (WPB) in the tectonic setting of volcanic arc basalts (Figure 18d). Based on geochemical studies in the study

https://doi.org/10.5281/zenodo.15130089

area, the samples have a bimodal composition with both mafic and acidic components. Consequently, some of the samples fall within the range of arc volcanic rocks; Th-Hf/3-Ta ternary diagram (Wood, 1979). The Ta/Yb vs. Th/Yb diagram (Pearce. 1983) (Figure 18e) shows that the volcanic rocks of Fathabad occur in subduction-related active continental margin tectonics. Accordingly, the magma of the Fathabad volcanic rocks originated from a source enriched in subduction components (SZ) and later developed by assimilation fractionation (AFC).

NATURE OF THE ORE-FORMING FLUIDS

The effective fluid density within the mineralization system is found to be between 0.99 and 1.13 g/cm^3 as shown in (Figure 19 b). This finding leads to an estimated pressure requirement for confining intermediate fluid loads within the quartz and calcite veins of between 2 and 50 bar (Figure 19 b). Further examination of the homogenization temperature and salinity diagram (Figure 19a) suggests a limited degree of mixing between secondary magmatic fluids and atmospheric fluids. Such interaction suggests a significant dilution effect of atmospheric fluid on magmatic constituents, facilitating the deposition of metals such as copper and gold, along with magmatic sulfur within the veins. Research highlighted by Seward (1973) and Seward et al. (2013), highlights the dominance of bisulfide complexes in environments with reduced conditions and temperatures below 300°C. This is supported by fluid samples with low to medium salinity and formation temperatures below this threshold (Figure 19 a, b), suggesting that bisulfide complexes play a key role in vein mineralization at the Fathabad deposit.

In addition, (Figure 19b) shows the trends in salinity and homogenization temperature for intermediate fluid loads, emphasizing the importance of isothermal mixing and dilution with surface fluids in copper deposition by bisulfide complexes. Analysis of primary inclusions reveals eutectic temperatures between -41 and -52 °C, indicative of hydrothermal fluids rich in $CaCl_2$ and NaCl. These conditions are consistent with the $H_2O+NaCl+CaCl_2$ fluid dominance of Shepherd et al. (1985) with homogenization temperatures ranging from 85 to 210 °C (mean 150 °C). Homogenization temperatures of L+V FIs trapped in the quartz and calcite veins indicate that quartz formed mainly between 85 and 210 °C and calcite between 135 and 208 °C. L+V fluid inclusion (FI) analysis reveals formation temperatures for quartz and calcite, suggesting parallels with epithermal precious and base metal deposits (Simmons et al., 2005).

Figure (18a, b) illustrates the evolution trend of the ore-forming fluids at medium to low homogenization temperature and salinity in the $H_2O+NaCl+CaCl_2$ system. The salinity versus homogenization temperature plot of Beane (1983) (Figure 19a) attributes the mineralization of the Fathabad deposit to mixing of basinal brines with magmatic fluid. This mixing, detailed in (Figure 19b), is emerging as a key process in the formation of large hydrothermal ore deposits, along with cooling and surface fluid dilution (Cooke and McPhail, 2001). The mixing of magmatic fluids with meteoric water (Figure 19a) reduced the salinity and temperature of the ore-forming fluids, resulting in the precipitation of metallic elements in the Fathabad deposit (Pirajno, 2009). According to (Figure 19b), surface fluid dilution, cooling and mixing can play an important role in the precipitation of ore-forming minerals; however, the role of surface fluid dilution and cooling

https://doi.org/10.5281/zenodo.15130089

is dominant (Figure 19b). Furthermore, the absence of steam-rich inclusions suggests that boiling played a negligible role in metal deposition within the Fathabad deposit. Quartz veins containing chalcopyrite and pyrite were identified along with disseminated copper mineralization. The process of silicification consumed significant OH^- and SiO_2 within the system during mineralization, resulting in the fluid becoming acidic with elevated levels of H^+ and $S2^-$.

These physicochemical changes in the fluid system provided favorable conditions for subsequent sulfide ore precipitation. During the addition of meteoric water to the ore-forming system, the gradual cooling, dilution and mixing of the fluids leads to an increase in acidity and oxidation of the ore-forming rocks and rapid deposition of sulfide minerals in the faults and fractures of the volcanic host rocks. As there are no boiling accumulations in the hydrothermal system, the homogenization temperatures are not interpreted to be close to the trapping temperatures (Roedder and Bodnar, 1980). The pressure (<20 bar) of the low to medium salinity LV FIs can be used to estimate the approximate pressure of the ore-forming fluids (Appendix Table 3; Figure 19b). L+V FIs are characterized by low pressures (between 1 and <20 bar; Figure 19b), indicating that they formed near the surface (< 0.1 km), suggesting that the ore minerals and coexisting quartz and calcite veins formed at shallow depths in an open environment.

SOURCE OF SULFUR

The study of stable sulfur isotopes in geology provides valuable insights into the origin of sulfur and the conditions conducive to the formation of sulfide ores. $\delta^{34}S$ values in chalcopyrite within mineralized quartz veins of the porphyry andesite deposit at Fathabad range from -1.58‰ to -2.86‰ per thousand (Appendix Table 5). These values indicate the direct involvement of sulphurous fluids derived from a magmatic source (Chaussidon et al., 1989). These results are consistent with the magmatic origin of sulfur observed in hydrothermal deposits δ^34S ~ 0‰ (Ohmoto and Rye, 1979). At temperatures below 400 degrees Celsius, the dominant sulfur species in the hydrothermal system is H_2S resulting from sulfur reduction (Ohmoto and Rye, 1979). The $\delta^{34}S$ values of H_2S in equilibrium with chalcopyrite (-1/1‰ to -3.15‰) further confirm the presence of reduced sulfur in the form of H_2S in the hydrothermal fluid. This reductive sulfur ligand plays a crucial role in facilitating the transfer of copper metal during chalcopyrite deposition under hydrothermal conditions.

In addition, the interaction of magmatic-hydrothermal gases such as HCl and SO_2 leads to the instability of SO_2 and subsequent acidification of the solution. The resulting formation of H_2SO_4 and H_2S is as follows $4SO_2 + 4H_2O = 3H_2SO_4 + H_2S$. This acidity is subsequently neutralized by reactions with the host rock, resulting in a complex interplay of chemical changes (Joun et al., 2018). Fluid mixing, involving magma with acidic pH and atmospheric waters with higher pH and temperature, further contributes to the reduction of metal complex solubility. Ultimately, this process promotes metal enrichment and deposition within the geological system (Tindell et al., 2018).

TYPE OF DEPOSIT

https://doi.org/10.5281/zenodo.15130089

The Fathabad district has a wide but subtle alteration pattern. The exposed rocks have undergone varying degrees of alteration at different stages. In the eastern part of the range there is a wide zone of alteration, mainly concentrated around the intrusive mass. The intensity of alteration gradually decreases as it extends towards the sedimentary rocks. Observations within the study area indicate that the latitic andesite units in the eastern part have undergone some clay-chlorite alteration. There is also limited silicification in this area, occasionally accompanied by black tourmaline veinlets. In particular, the surveyed area shows evidence of mineralized silica solution resulting in the formation of silica veins (often mineralized) up to 1.5 meters thick across all sedimentary volcanic units. The highest concentration of these veins and siliceous structures occurs within the volcanic host unit (ranging from latite andesite to porphyritic andesite). In addition, strong alteration and traces of chalcopyrite and gold mineralization have been deposited along the primary faults branching off the inner fault within siliceous veins filled with iron and manganese oxides in both volcanic and conglomerate units.

The characteristics of the host rock, which is of volcanic origin, its proximity to intrusive masses and its association with alteration processes suggest that the mineralization observed is of epithermal nature. Siliceous alteration is particularly significant in this regard. The primary mineralization is sulfides and there is a clear link between the mineralization and geological structures such as faults. Geochemical studies and the analysis of numerous samples from different ore intervals show anomalies in gold, silver, arsenic, antimony, lead, zinc and other heavy metals. These elements are typically associated with epithermal systems (Appendix Table 4).

CONCLUSION

The Fathabad Cu±Au deposit is located in the Khaf-Kashmar-Bardaskan Metallogenic Belt (KKBMB) in northeastern Iran. It is hosted by Eocene volcanic units, including basaltic andesite, rhyolite and trachyandesite lavas, which have been intensely replaced, dissolved and brecciated during hydrothermal alteration. Cu-Au mineralization is structurally controlled by NE-SW trending minor faults associated with the Dorouneh fault system. Silicification, argillic, sericitization, carbonatization, Fe-oxide-hydroxide and propylitization are the main alterations observed in the study area. Mineralization in the Fatahabad district has been classified as hypogene (pyrite, chalcopyrite and magnetite) and supergene (chalcocite, bornite, covellite, malachite, hematite, goethite and limonite). Gangue minerals include quartz, calcite, epidote, chlorite and albite.

The volcanic rocks of Fathabad are partly metaluminous to mostly peraluminous and belong to the high-K calc-alkaline and shoshonitic series. The negative correlation of Fe_2O_3, MgO, P_2O_5, Al_2O_3 and Eu/Eu* with SiO_2 can be interpreted by fractionation of the minerals magnetite, hornblende, apatite, plagioclase and biotite. The Fathabad volcanics, characterized by low Y and Yb_N and high Sr content and high $(La/Yb)_N$ ratios, have similar geochemical characteristics to the adakites. The strong to weak negative Eu anomaly and high Sr/Y ratio of the Fathabad volcanic samples indicate high oxygen fugacity and water content. Geochemical features such as enrichment of LREE and LILE with depletion of HREE and HFSE, and a high Th/Yb ratio indicate the formation of volcanic rocks on a subduction-related and active continental margin in an extensional environment. From the geological and geochemical analysis presented in this study, we conclude that the volcanic rocks were probably formed by varying degrees of partial melting of a garnet-bearing lherzolite (garnet>spinel) from the metasomatized mantle under conditions of high oxygen fugacity. They were enriched by subduction components (SZ) and later developed by assimilation fractionation (AFC). Microthermometry of the primary LV FIs shows that the ore-forming fluids are dominated by the H_2O-NaCl+$CaCl_2$ fluid system with homogenization temperatures between 85 and 210 °C and salinities between 4.74 and 23.05 wt.% NaCl equiv. The mixing of basinal brines with magmatic-meteoric mixing reduced the salinity and temperature of the ore-forming fluids - dilution, cooling and mixing of surface fluids may play a role in the precipitation of ore-forming minerals.

Geochemical analysis of sulfur isotopes in chalcopyrite provides evidence for a magmatic origin of sulfur, emphasizing the predominance of reduced sulfur species, particularly hydrogen sulfide (H_2S), in the hydrothermal fluids. Study of fluid inclusions and sulfur isotopes of chalcopyrite within quartz veins demonstrates the interaction and regeneration of mineralizing hydrothermal fluids with the host rocks, with mixing of magmatic and hydrothermal fluids with atmospheric fluids. During their migration, ore-forming fluids interact with the host rock and promote the leaching of rare earth elements (REEs) and metal elements from the host rock as a result of decreasing temperature and solubility of the bisulfide complex.

Consequently, volcanic rocks are identified as the primary source of metal elements critical for mineralization. Therefore, through extensive geological studies, an understanding of the structural controls on mineralization and alteration, the geochemistry of the ore veins and the properties of the ore-forming hydrothermal fluids, the Fathabad deposit is classified as a representative case of epithermal gold-bearing vein copper mineralization (Appendix Table 4).

ACKNOWLEDGEMENTS

This paper is part of the first author's Ph.D. thesis at the Islamic Azad University of Mahallat, Markazi Province, Iran. The Iranian Mines and Mining Industries Development and Renovation Organization (IMIDRO) is thanked for supporting the analyses of the present work. The reviewers of the journal are gratefully acknowledged for their constructive comments and suggestions for the revision of the manuscript.

REFERENCES

Aghanabati S. A., 2013. Geology of Iran. Geological Survey of Iran 587p.

Alaminia Z., Karimpour M.H., Homam S.M., Finger F., 2013. The magmatic record in the Arghash region (northeast Iran) and tectonic implications. International Journal of Earth Sciences 102, 1603-1625. https://doi.org/10.1007/s00531-013-0897-1

Alaminia Z., Karimpour, M.H., Haidarian M.R., 2010. The cheshmeh Noghreh abandoned mine: Type of Epithermal Au-Cu Mineralization in the Northwest of kashmar, Iran. In 1st International Applied Geological Congress, Department of Geology.

Alavi M., 1991. Sedimentary and structural characteristics of the Paleo-Tethys remnants in northeastern Iran. Geological Society of America Bulletin 103(8), 983-992. https://doi.org/10.1130/0016-7606(1991)103%3C0983:SASCOT%3E2.3.CO;2

Alavi M., 2004. Regional stratigraphy of the Zagros fold-thrust belt of Iran and its proforeland evolution. American journal of Science 304(1), 1-20. http://dx.doi.org/10.2475/ajs.304.1.1

Aldanmaz E., Pearce J.A., Thirlwall M.F., Mitchell J.G., 2000. Petrogenetic evolution of late Cenozoic, post-collision volcanism in western Anatolia, Turkey. Journal of volcanology and geothermal research 102(1-2), 67-95. https://doi.org/10.1016/S0377-0273(00)00182-7

Arjmandzadeh R., Alirezaei S., Almasi A., 2022. Tectonomagmatic reconstruction of the Upper Mesozoic-Cenozoic Neotethyan arcs in the Lut block, East Iran: a review and synthesis. Turkish Journal of Earth Sciences 31(6), 520-544. https://doi.org/10.55730/1300-0985.1818

Asiabanha A. and Foden J., 2012. Post-collisional transition from an extensional volcano-sedimentary basin to a continental arc in the Alborz Ranges, N-Iran. Lithos 148, 98-111. https://doi.org/10.1016/j.lithos.2012.05.014

Ballard J.R., Palin J.M., Campbell I.H., 2002. Relative oxidation states of magmas inferred from Ce (IV)/Ce (III) in zircon: application to porphyry copper deposits of northern Chile. Contributions to Mineralogy and Petrology 144(3), 347-364. https://doi.org/10.1007/s00410-002-0402-5

Barton M.D., 2014. Iron oxide (–Cu–Au–REE–P–Ag–U–Co) systems. Treatise on geochemistry 515–541.

Barton M.D., Johnson D.A., 2004. Footprints of Fe-oxide (-Cu-Au) systems. University of Western Australia Special Publication 33, 112-116.

Beane R.E., 1983. The magmatic-meteoric transition. Geothermal Resources Council Special Report 13, 245-253.

Berberian M., King G.C.P., 1981. Towards a paleogeography and tectonic evolution of Iran. Canadian journal of earth sciences 18(2), 210-265. https://doi.org/10.1139/e81-019

Biabangard H., Boomeri M., Taimouri K., Mohammadpour F., 2017. Petrography, alteration and genesis of iron mineralization in Roshtkhar. Journal of Economic Geology 9(1), 93-115. https://doi.org/10.22067/econg.v9i1.47297

Billström K., Eilu P., Martinsson O., Niiranen T., Broman C., Weihed P., Ojala J., 2011. IOCG and related mineral deposits of the northern Fennoscandian Shield.

Bodnar R.J., 1993. Revised equation and table for determining the freezing point depression of H2O-NaCl solutions. Geochimica et Cosmochimica acta 57(3), 683-684. https://doi.org/10.1016/0016-7037(93)90378-A

Bonin B., 2004. Do coeval mafic and felsic magmas in post-collisional to within-plate regimes necessarily imply two contrasting, mantle and crustal, sources? A review. Lithos 78(1-2), 1-24. https://doi.org/10.1016/j.lithos.2004.04.042

Boroozinyat B., malekzadeh Shafaroudi A., Haidarian Shahri M., 2019. Mineralogy, geochemistry, and fluid inclusion studies in Zaveh copper mineralization occurrence, southeast of Torbat-e-Hydarieh. Iranian Journal of Crystallography and Mineralogy. http://dx.doi.org/10.29252/ijcm.27.1.3

Brown P.E., 1989. FLINCOR; a microcomputer program for the reduction and investigation of fluid-inclusion data. American Mineralogist 74(11-12), 1390-1393.

Brown P.E., Lamb W.M., 1989. PVT properties of fluids in the system H_2O±CO_2±NaCl: New graphical presentations and implications for fluid inclusion studies. Geochimica et Cosmochimica Acta 53(6), 1209-1221. https://doi.org/10.1016/0016-7037(89)90057-4

Camp V.E., Griffis R.J., 1982. Character, genesis and tectonic setting of igneous rocks in the Sistan suture zone, eastern Iran. Lithos 15(3), 221-239. https://doi.org/10.1016/0024-4937(82)90014-7

Castro A., Aghazadeh M., Badrzadeh Z., Chichorro M., 2013. Late Eocene–Oligocene post-collisional monzonitic intrusions from the Alborz magmatic belt, NW Iran. An example of monzonite magma generation from a metasomatized mantle source. Lithos 180, 109-127. https://doi.org/10.1016/j.lithos.2013.08.003

Chaussidon M., Albarède F., Sheppard S.M., 1989. Sulphur isotope variations in the mantle from ion microprobe analyses of micro-sulphide inclusions. Earth and Planetary Science Letters 92(2), 144-156. https://doi.org/10.1016/0012-821X(89)90042-3

Chen W., Zhao X.F., Li X.C., Zhou M.F., 2019. An overview on the characteristics and origin of iron-oxide copper gold (IOCG) deposits in China. Acta Petrologica Sinica 35(1), 99-118. http://dx.doi.org/10.18654/1000-0569/2019.01.07

Childress T.M., Simon A.C., Day W.C., Lundstrom C.C., Bindeman I.N., 2016. Iron and oxygen isotope signatures of the Pea Ridge and Pilot Knob magnetite-apatite deposits, southeast Missouri, USA. Economic Geology 111(8), 2033-2044. https://doi.org/10.2113/econgeo.111.8.2033

Cooke D.R., McPhail D.C., 2001. Epithermal Au-Ag-Te mineralization, Acupan, Baguio district, Philippines: numerical simulations of mineral deposition. Economic Geology, 96(1), 109-131. https://doi.org/10.2113/gsecongeo.96.1.109

Corriveau L.C., Potter E.G., Acosta-Gongora P.A., Blein O., Montreuil J.F.F., de Toni A.A., Hanes R., 2017. Petrological mapping and chemical discrimination of alteration facies as vectors to IOA, IOCG, and affiliated deposits within Laurentia and beyond. In SGA Québec 2017.

Dare S.A., Barnes S.J., Beaudoin G., 2015. Did the massive magnetite “lava flows” of El Laco (Chile) form by magmatic or hydrothermal processes? New constraints from magnetite composition by LA-ICP-MS. Mineralium Deposita 50, 607-617. https://doi.org/10.1007/s00126-014-0560-1

Day W.C., Slack J.F., Ayuso R.A., Seeger, C.M., 2016. Regional geologic and petrologic framework for iron oxide±apatite±rare earth element and iron oxide copper-gold deposits of the Mesoproterozoic St. Francois Mountains terrane, southeast Missouri, USA. Economic Geology 111(8), 1825-1858. https://doi.org/10.2113/econgeo.111.8.1825

de Melo G.H., Monteiro L.V., Xavier R.P., Moreto C.P., Arquaz R.M., Silva M.A.D., 2019a. Evolution of the Igarapé Bahia Cu-Au deposit, Carajás province (Brazil): early syngenetic chalcopyrite overprinted by IOCG mineralization. Ore geology reviews 111, 102993. https://doi.org/10.1016/j.oregeorev.2019.102993

de Melo G.H., Monteiro L.V., Xavier R.P., Moreto C.P., Santiago E., 2019b. Tracing fluid sources for the Salobo and Igarapé Bahia deposits: implications for the genesis of the iron oxide copper-gold deposits in the Carajás Province, Brazil. Economic Geology 114(4), 697-718. https://doi.org/10.5382/econgeo.4659

deMelo G.H., Monteiro L.V., Xavier R.P., Moreto C.P., Santiago E.S., Dufrane S.A., Santos A.F., 2017. Temporal evolution of the giant Salobo IOCG deposit, Carajás Province (Brazil): constraints from paragenesis of hydrothermal alteration and U-Pb geochronology. Mineralium Deposita 52, 709-732. https://doi.org/10.1007/s00126-016-0693-5

Defant M.J., Drummond M.S., 1990. Derivation of some modern arc magmas by melting of young subducted lithosphere. nature, 347(6294), 662-665. https://doi.org/10.1038/347662a0

Ebrahimi S., Arabamiri A., Ghanbari H., 2020. Mineralogy, alteration, fluid inclusion and stable isotopes studies of the Sharifabad-Bardeskan copper deposit, NE Iran. Scientific Quarterly Journal of Geosciences 30(117), 135-146. https://doi.org/10.22071/gsj.2020.197243.1687

Esmaeili Sevieri A., Karimpour M.H., Malekzadeh Shafaroudi A., Mahboubi A., Song Y., 2019. Irankuh lead-zinc mining district, southern Isfahan, Iran: Evidences of geology, fluid inclusion and isotope geochemistry. Periodico di Mineralogia 78, 254-267. https://doi.org/10.2451/2019PM867

Förster H.J., Tischendorf G., Trumbull R.B., 1997. An evaluation of the Rb vs. (Y+ Nb) discrimination diagram to infer tectonic setting of silicic igneous rocks. Lithos 40(2-4), 261-293. https://doi.org/10.1016/S0024-4937(97)00032-7

Frietsch R., Tuisku P., Martinsson O., Perdahl J.A., 1997 Early proterozoic Cu□(Au) and Fe ore deposits associated with regional Na-Cl metasomatism in northern Fennoscandia. Ore geology reviews 12(1), 1-34. https://doi.org/10.1016/S0169-1368(96)00013-3

Ghasemi Siani M.G., Mehrabi, B., Neubauer F., Zhang R., Cao S., 2022. Geochronology and geochemistry of zircons from fertile and barren intrusions in the Sangan mining area (NE Iran): Implications for tectonic setting and mineral exploration. Journal of Asian Earth Sciences 233, 105243. https://doi.org/10.1016/j.jseaes.2022.105243

Golmohammadi A., Karimpour M.H., Shafaroudi A.M., Mazaheri S.A., 2015. Alteration-mineralization, and radiometric ages of the source pluton at the Sangan iron skarn deposit, northeastern Iran. Ore Geology Reviews 65: 545-563. https://doi.org/10.1016/j.oregeorev.2014.07.005

Golmohammadi A., Mazaheri S.A., Shafaroudi A.M., Karimpour M.H., 2014. Zircon U-Pb dating and geochemistry of Sarkhar and Bermani granitic rocks, East of Sangan iron mine, Khaf. Petrology (2228-5210), 5(17).

Golonka J., 2004. Plate tectonic evolution of the southern margin of Eurasia in the Mesozoic and Cenozoic. Tectonophysics 381(1-4), 235-273. https://doi.org/10.1016/j.tecto.2002.06.004

Gorton M.P., Schandl E.S., 2000. From continents to island arcs: a geochemical index of tectonic setting for arc-related and within-plate felsic to intermediate volcanic rocks. The Canadian Mineralogist 38(5), 1065-1073. https://doi.org/10.2113/GSCANMIN.38.5.1065

Groves D.I., Bierlein F.P., Meinert L.D., Hitzman M.W., 2010. Iron oxide copper-gold (IOCG) deposits through Earth history: Implications for origin, lithospheric setting, and distinction from other epigenetic iron oxide deposits. Economic Geology 105(3), 641-654. https://doi.org/10.2113/gsecongeo.105.3.641

Gudnason J., Holm, P.M., Søager N., Llambías E.J., 2012. Geochronology of the late Pliocene to recent volcanic activity in the Payenia back-arc volcanic province, Mendoza Argentina. Journal of South American Earth Sciences 37, 191-201. https://doi.org/10.1016/j.jsames.2012.02.003

Guilbert J.M. and Park J.R., 1986. The geology of ore deposits. Freeman and company. New York 985 pp.

Hawkins T., Herrington R., Smith M., Maslenikov V., Boyce A., 2012. The iron skarns of the Turgai Belt, northwestern Kazakhstan. In Hydrothermal iron oxide copper-gold and related deposits: a global perspective (pp. 461-474). PGC publishing.

Haynes D.W. and Porter T.M., 2000. Iron oxide copper (-gold) deposits: their position in the ore deposit spectrum and modes of origin. Hydrothermal Iron Oxide Copper-Gold & related deposits. a global perspective (Porter, TM, 71-90.

Hayward N., Skirrow R.G., Porter T.M., 2010. Geodynamic setting and controls on iron oxide Cu-Au (±U) ore in the Gawler Craton, South Australia. Hydrothermal iron oxide copper-gold and related deposits: A global perspective 3, 105-131.

He Y., Li S., Hoefs J., Huang F., Liu S.A., Hou Z., 2011. Post-collisional granitoids from the Dabie orogen: new evidence for partial melting of a thickened continental crust. Geochimica et cosmochimica acta 75(13), 3815-3838. https://doi.org/10.1016/j.gca.2011.04.011

Hedenquist J.W., Thompson J.F., Goldfarb R.J., Richards J.P., 2005. One Hundredth Anniversary Volume. Economic Geology, Society of Economic Geologists.

Hitzman M.W., 2000. Iron oxide-Cu-Au deposits: what, where, when, and why. In: Porter T.M. (ed.), hydrothermal iron oxide copper-gold and related deposits: a global perspective. Adelaide, Australian Mineral Foundation, 9–25.

Hitzman M.W., Oreskes N., Einaudi M.T., 1992. Geological characteristics and tectonic setting of proterozoic iron oxide (Cu+ U+ Au+ REE) deposits. Precambrian research 58(1-4), 241–287. https://doi.org/10.1016/0301-9268(92)90121-4

Hollocher K., Robinson P., Walsh E., Roberts D., 2012. Geochemistry of amphibolite-facies volcanics and gabbros of the Støren Nappe in extensions west and southwest of Trondheim, Western Gneiss Region, Norway: a key to correlations and paleotectonic settings. American Journal of Science 312(4), 357-416. https://doi.org/10.2475/04.2012.01

Hosseinzadeh M., Maghfouri S., Moayyed M., Rahmani A., 2015. geology, mineralogy and Geochemistry of the epithermal copper (gold) deposit of Khalifahlu, Tarem area, north of Khorramdara.- 18th conference of the associationGeology of Iran, Tarbiat Modares University.

Huang X.W., Boutroy É., Makvandi S., Beaudoin G., Corriveau L., De Toni A.F., 2019. Trace element composition of iron oxides from IOCG and IOA deposits: relationship to hydrothermal alteration and deposit subtypes. Mineralium Deposita 54, 525-552. https://doi.org/10.1007/s00126-018-0825-1

Hunger R.B., Xavier R.P., Moreto C.P.N., Gao J.F., 2018. Hydrothermal alteration, fluid evolution, and Re-Os geochronology of the Grota Funda iron oxide copper-gold deposit, Carajas Province (Para State), Brazil. Economic Geology 113(8), 1769-1794. https://doi.org/10.5382/econgeo.2018.4612

Ja P., 1983. Role of the sub-continental lithosphere in magma genesis at active continental margins. Continental basalts and mantle xenoliths 230-249.

Javadi H.R., Ghassemi M.R., Shahpasandzadeh M., Guest B., Ashtiani M.E., Yassaghi A.L., Kouhpeyma M., 2013. History of faulting on the Doruneh Fault System: Implications for the kinematic changes of the Central Iranian Microplate. Geological Magazine 150(4), 651-672. https://doi.org/10.1017/S0016756812000751

Javidi Moghaddam M., Karimpour M.H., Malekzadeh Shafaroudi A., 2020. Rashidi copper vein deposit, North Khur, Eastern Iran: hydrothermal alteration, mineralization, geochemistry, fluid inclusion and stable isotope investigations. Scientific Quarterly Journal of Geosciences 29(116), 265-276. https://doi.org/10.22071/gsj.2019.128676.1460

Javidi Moghaddam M., Karimpour M.H., Malekzadeh Shafaroudi A., Santos J.F., Corfu F., 2021. Middle Eocene magmatism in the Khur region (Lut Block, Eastern Iran): implications for petrogenesis and tectonic setting. International Geology Review 63(9): 1051-1066. https://doi.org/10.1080/00206814.2019.1708815

John D., Vikre P.G., du Bray E.A., Blakely R.J., Fey D.L., Rockwell B.W., Graybeal F., 2018. Descriptive models for epithermal gold-silver deposits. U.S. Geological Survey Scientific Investigations Report 2010–5070, 247. https://doi.org/10.3133/sir20105070Q

Karimpour M.H., 2003. Mineralogy, alteration, origin rock and tectonic environment of Iron-Oxides Cu-Au deposits and examples from Iran, 11th Crystallography and Mineralogy Conference of Iran, Yazd University 184–189p (in persian).

Karimpour M.H., 2005. Cu-Au mineralization along with magnetite-specularite (IOCG) and examples from Iran, Proceedings of the 9th Iran Geological Conference, Tarbiat Moalem University, Tehran (in persian).

Karimpour M.H., Shafaroudi A.M., Bajestani A.M., Schader R.K., Stern C.R., Farmer L., Sadeghi M., 2017. Geochemistry, geochronology, isotope and fluid inclusion studies of the Kuh-e-Zar deposit, Khaf-Kashmar-Bardaskan magmatic belt, NE Iran: Evidence of gold-rich iron oxide–

copper–gold deposit. Journal of Geochemical Exploration 183, 58-78. https://doi.org/10.1016/j.gexplo.2017.10.001

Karimpour M.H. and Malekzadeh Shafaroudi A., 2006. Comparison of the geochemistry of source rocks at Tannurjeh Au-bearing magnetite and Sangan Au-free magnetite deposits, Khorasan Razavi, Iran. Iranian Journal of Crystallography and Mineralogy 13(1), 3-26.

Kazemi M., 2016. Economic Geology Report of Fathabad Roshtkhar Region (Parsikankav Company) 101p. (in persion).

Kazemi Z., Ghasemi H., Tilhac R., Griffin W., Moghadam H.S., O'Reilly S., Mousivand F., 2019. Late Cretaceous subduction-related magmatism on the southern edge of Sabzevar basin, NE Iran. Journal of the Geological Society 176(3), 530-552. https://doi.org/10.1144/jgs2018-076

Khazaei E., Mahmoudy-Gharaie M.H., Mahboubi A., Moussavi-Harami R., Taheri J., 2018. Petrography, major and trace elemental geochemistry of the Ordovician-Silurian siliciclastics in north of Tabas Block, Central Iran: Implications for provenance and paleogeography. Journal of Sciences, Islamic Republic of Iran 29(2), 129-142. https://doi.org/10.22059/jsciences.2018.65019

Kholghii-Khasraghii M.H., 1990. Geological Map of the Dolat Abad, Scale 1:100000, Geological Survey of Iran.

LE MAITRE R.W., 2002. Igneous Rocks: A Classification and Glossary of Terms: Recommendations of the International Union of Geological Sciences Subcommission on the Systematics of Igneous Rocks. Cambridge University Press. https://doi.org/10.1017/CBO9780511535581

Leão-Santos M., Moraes R., Li Y., Raposo M.I., Zuo B., 2022. Hydrothermal Alteration Zones' Magnetic Susceptibility Footprints and 3D Model of Iron Oxide-Copper-Gold (IOCG) Mineralization, Carajás Mineral Province, Brazil. Minerals 12(12), 1581. https://doi.org/10.3390/min12121581

Li B., Jiang S.Y., 2015. A subduction-related metasomatically enriched mantle origin for the Luoboling and Zhongliao Cretaceous granitoids from South China: implications for magma evolution and Cu–Mo mineralization. International Geology Review 57(9-10), 1239-1266. https://doi.org/10.1080/00206814.2014.979452

Li H., Zhang Z., Liu B., Jin Y., Santosh M., 2023. The genetic link between iron oxide-apatite and iron skarn mineralization in the Beizhan deposit, Western Tianshan, NW China: Evidence from magnetite and gangue mineral geochemistry. Journal of Asian Earth Sciences 241, 105460. https://doi.org/10.1016/j.jseaes.2022.105460

Li X., Miao L., Zhang F., Ghasemi H., Zhu S., Yang S., 2019. Mashhad komatiitic rocks in NE Iran: Origin and implications for the evolution of the Paleo-Tethyan Ocean. Geological Journal 54(6), 3314-3334. https://doi.org/10.1002/gj.3329

Luo X., Xia Q.X., Zheng Y.F., Li W.C., 2022. An experimental study of partial melting of metafelsic rocks: Constraints on the feature of anatectic melts and the origin of garnets in collisional orogens. Journal of Earth Science 33(3), 753-769. https://doi.org/10.1007/s12583-021-1547-3

Maghfouri S., Rastad E., Mousivand F., Lin Y., Zaw K., 2016. Geology, ore facies and sulfur isotopes geochemistry of the Nudeh Besshi-type volcanogenic massive sulfide deposit, southwest Sabzevar basin, Iran. Journal of Asian Earth Sciences 125, 1-21. https://doi.org/10.1016/j.jseaes.2016.04.022

Malekzadeh Shafaroudi A, Karimpour M.H., 2015. Mineralogic, fluid inclusion, and sulfur isotope evidence for the genesis of Sechangi lead–zinc (–copper) deposit, Eastern Iran. Journal of African Earth Sciences 107, 1-14. https://doi.org/10.1016/j.jafrearsci.2015.03.015

Malekzadeh Shafaroudi A., Karimpour M.H., Golmohammadi A., 2013 Zircon U–Pb geochronology and petrology of intrusive rocks in the C-North and Baghak districts, Sangan iron mine, NE Iran. Journal of Asian Earth Sciences 64, 256-271. https://doi.org/10.1016/j.jseaes.2012.12.028

Maniar P.D. and Piccoli P.M., 1989. Tectonic discrimination of granitoids. Geological society of America bulletin 101(5), 635-643. https://doi.org/10.1130/0016-7606(1989)101%3C0635:TDOG%3E2.3.CO;2

Mazhari M.S., Saadat S., Mazaheri S.A., Homam S.M., Le Roux P., 2023. U-Pb Geochronological and Geochemical Characteristics of the Kalate-Naser Intrusive Rocks, Eastern Lut, Iran. Geopersia 13(1), 167-184.

Mazhari N., Shafaroudi A.M., Ghaderi M., Lackey J.S., Farmer G.L., Karimpour M.H., 2017. Geochronological and geochemical characteristics of fractionated I-type granites associated with the skarn mineralization in the Sangan mining region, NE Iran. Ore Geology Reviews 84, 116-133. https://doi.org/10.1016/j.oregeorev.2017.01.003

Mehrabi B., Ghasemi Siani M., Zhang R., Neubauer F., Lentz D.R., Fazel E.T., Shahraki B.K., 2021. Mineralogy, petrochronology, geochemistry, and fluid inclusion characteristics of the Dardvay skarn iron deposit, Sangan mining district, NE Iran. Ore Geology Reviews 134, 104146. https://doi.org/10.1016/j.oregeorev.2021.104146

Mehrabi B., Karimishahraki B., Banks D., Boyce A., Yardley B.W., 2019. Hydrothermal iron oxide-Cu-Au (IOCG) mineralization at the Jalal-Abad deposit, northwestern Zarand, Iran. Ore Geology Reviews 106, 300-317. https://doi.org/10.1016/j.oregeorev.2019.01.019

Metcalfe I., 2013. Gondwana dispersion and Asian accretion: Tectonic and palaeogeographic evolution of eastern Tethys. Journal of Asian Earth Sciences 66, 1-33. https://doi.org/10.1016/j.jseaes.2012.12.020

Moghaddam M.J., Karimpour M.H., Shafaroudi A.M., Santos J.F., Mendes M.H., 2019. Geochemistry, Sr-Nd isotopes and zircon U-Pb geochronology of intrusive rocks: Constraint on the genesis of the Cheshmeh Khuri Cu mineralization and its link with granitoids in the Lut Block, Eastern Iran. Journal of Geochemical Exploration 202, 59-76. https://doi.org/10.1016/j.gexplo.2019.04.001

Moreto C.P.N., Monteiro L.V.S., Xavier R.P., Creaser R.A., DuFrane S.A., Tassinari C.C.G., Amaral W.S., 2015. Neoarchean and Paleoproterozoic iron oxide-copper-gold events at the Sossego deposit, Carajás Province, Brazil: Re-Os and U-Pb geochronological evidence. Economic Geology 110(3), 809-835. https://doi.org/10.2113/econgeo.110.3.809

Mumin A.H., Corriveau L., Somarin A.K., Ootes L., 2007. Iron oxide copper-gold-type polymetallic mineralization in the Contact Lake belt, Great Bear magmatic zone, Northwest Territories, Canada. Exploration and Mining Geology 16(3-4), 187-208. https://doi.org/10.2113/gsemg.16.3-4.187

Nabatian G., Rastad E., Neubauer F., Honarmand M., Ghaderi M., 2015. Iron and Fe–Mn mineralisation in Iran: implications for Tethyan metallogeny. Australian Journal of Earth Sciences 62(2), 211–241. https://doi.org/10.1080/08120099.2015.1002001

Naranjo J.A., Henríquez F., Nyström J.O., 2010. Metasomatismo de contacto subvolcánico en el Complejo Volcánico El Laco, Andes centrales. Andean geology 37(1), 110-120. http://dx.doi.org/10.4067/S0718-71062010000100005

Ohmoto H. and Rye R.O., 1979. Isotopes of sulfur and carbon. In: Barnes, H.L. (Ed.), Geochemistry of Hydrothermal Ore Deposits. 2nd ed. Wiley, New York, 509 – 567.

Pearce J.A., Harris N.B., Tindle A.G., 1984. Trace element discrimination diagrams for the tectonic interpretation of granitic rocks. Journal of petrology 25(4), 956-983. https://doi.org/10.1093/PETROLOGY/25.4.956

Peccerillo A. and Taylor S.R., 1976. Geochemistry of Eocene calc-alkaline volcanic rocks from the Kastamonu area, northern Turkey. Contributions to mineralogy and petrology 58, 63-81. https://doi.org/10.1007/BF00384745

Pirajno F., 2009. Hydrothermal Processes and Mineral System. Springer, Australia 1273 pp.

Pollard P.J., 2006. An intrusion-related origin for Cu–Au mineralization in iron oxide–copper–gold (IOCG) provinces. Mineralium Deposita 41, 179-187. https://doi.org/10.1007/s00126-006-0054-x

Raeisi D., Hajsadeghi S., Hosseinzadehsabeti E., Babazadeh S., Lentz D.R., Santosh M., 2023. Exploration targeting in the Shadan porphyry gold–copper deposit, Lut block, Iran: Analysis of spatial distribution of sheeted veins and Lithogeochemical data. Minerals 13(4), 471. https://doi.org/10.3390/min13040471

Ramezani J. and Tucker R.D., 2003. The Saghand region, central Iran: U-Pb geochronology, petrogenesis and implications for Gondwana tectonics. American journal of science 303(7), 622-665.

Rashidi A., Khatib M.M., Nilfouroushan F., Derakhshani R., Mousavi S.M., Kianimehr H., Djamour Y., 2019. Strain rate and stress fields in the West and South Lut block, Iran: Insights from the inversion of focal mechanism and geodetic data. Tectonophysics 766, 94-114. https://doi.org/10.1016/j.tecto.2019.05.020

Rashidi A., Kianimehr H., Shafieibafti S., Mehrabi A., Derakhshani R., 2021. Active faults in the west of the Lut block (Central Iran). Geophys. Res 22, 70-84. https://doi.org/10.21455/gr2021.3-5

Rashidi A., Kianimehr H., Yamini-Fard F., Tatar M., Zafarani H., 2022. Present stress map and deformation distribution in the NE Lut block, Eastern Iran: Insights from seismic and geodetic strain and moment rates. Pure and Applied Geophysics 179(5), 1887-1917. https://doi.org/10.1007/s00024-022-03015-x

Richards J.P., 2003. Tectono-magmatic precursors for porphyry Cu-(Mo-Au) deposit formation. Economic geology 98(8), 1515-1533. https://doi.org/10.2113/gsecongeo.98.8.1515

Richards J.P., 2011. High Sr/Y arc magmas and porphyry Cu±Mo±Au deposits: Just add water. Economic Geology 106(7), 1075-1081. https://doi.org/10.2113/econgeo.106.7.1075

Roedder E. and Bodnar R.J., 1980. Geologic pressure determinations from fluid inclusion studies. Annual Review of Earth and Planetary Sciences 263 (8), 263. https://doi.org/10.1146/annurev.ea.08.050180.001403

Saadat S. and Stern C., 2016. Distribution and geochemical variations among paleogene volcanic rocks from the north-central Lut block, eastern Iran. Iranian Journal of Earth Sciences 8(1), 1-24.

Sepidbar F., Mirnejad H., Li J.W., Ma C., 2017. Mineral and stable isotope compositions, phase equilibria and 40Ar–39Ar geochronology from the iron skarn deposit in Sangan, northeastern Iran. Ore Geology Reviews 91, 660-681. https://doi.org/10.1016/j.oregeorev.2017.08.029

Sepidbar F., Mirnejad H., Ma C., Moghadam H.S., 2018. Identification of Eocene-Oligocene magmatic pulses associated with flare-up in east Iran: Timing and sources. Gondwana Research 57, 141-156. https://doi.org/10.1016/j.gr.2018.01.008

Sepidbar F., Moghadam H.S., Zhang L., Li J.W., Ma J., Stern R.J., Lin C., 2019. Across-arc geochemical variations in the Paleogene magmatic belt of Iran. Lithos 344, 280-296. https://doi.org/10.1016/j.lithos.2019.06.022

Seward T.M., 1973. Thio complexes of gold and the transport of gold in hydrothermal ore solutions. Geochimica et cosmochimica Acta 37(3), 379-399. https://doi.org/10.1016/0016-7037(73)90207-X

Seward T.M. and Barnes H.L., 1997. Metal transport by hydrothermal are fluid. In: H.L. Barnes (Editor), Geochemistry of Hydrothermal ore deposits. John Wiley and Sons, New York 435-486.

Shafaroudi A.M., Karimpour M.H., Golmohammadi A., 2013. Zircon U–Pb geochronology and petrology of intrusive rocks in the C-North and Baghak districts, Sangan iron mine, NE Iran. Journal of Asian Earth Sciences 64, 256-271. https://doi.org/10.1016/j.jseaes.2012.12.028

Shepherd T., Rankin A., alderton D., 1985. A practical guide to fluid inclusion studies.- Print Book, English, 1985, Blackie ; Distributed in the USA by Chapman and Hall, Glasgow New York.

Sillitoe R.H., 2003. Iron oxide-copper-gold deposits: an Andean view. Mineralium Deposita, 38, 787-812. https://doi.org/10.1007/s00126-003-0379-7

Sillitoe R.H. and BURROWS D.R., 2003. New field evidence bearing on the origin of the El Laco magnetite deposit, northern Chile—A reply. Economic Geology 98(7), 1501-1502. https://doi.org/10.2113/gsecongeo.97.5.1101

Simon A.C., Knipping J., Reich M., Barra F., Deditius A.P., Bilenker L., Childress T., 2018. Kiruna-type iron oxide-apatite (IOA) and iron oxide copper-gold (IOCG) deposits form by a combination of igneous and magmatic-hydrothermal processes: Evidence from the Chilean iron belt. https://doi.org/10.5382/SP.21.06

Skirrow R.G., 2022. Iron oxide copper-gold (IOCG) deposits–A review (part 1): Settings, mineralogy, ore geochemistry and classification. Ore Geology Reviews 140, 104569. https://doi.org/10.1016/j.oregeorev.2021.104569

Skirrow R.G., Davidson G.J., 2007. A special issue devoted to Proterozoic iron oxide Cu-Au-(U) and gold mineral systems of the Gawler Craton: preface. Economic Geology 102(8), 1373-1375.

Stampfli G.M. and Borel G.D., 2002. A plate tectonic model for the Paleozoic and Mesozoic constrained by dynamic plate boundaries and restored synthetic oceanic isochrons. Earth and Planetary science letters 196(1-2), 17-33. https://doi.org/10.1016/S0012-821X(01)00588-X

Sun J.B., Chen W., Liu X., Zhang Y., 2012. Ar-Ar and zircon U-Pb dating of quartz Albitophyres in the Hongshi Gold Ore District of Eastern Tianshan and Its Metallogenic significance.- Acta Geosci. Sin. 33, 907-917 (in Chinese with English abstract)

Sun S.S. and McDonough W.F., 1989. Chemical and isotopic systematics of oceanic basalts: implications for mantle composition and processes. Geological Society, London, Special Publications 42(1), 313-345. https://doi.org/10.1144/GSL.SP.1989.042.01.19

Sun Y.Z., Qiu K.F., An M.G., Li S.S., Shang Z., Wang Y., 2022. Geochronological and Geochemical Constraints on the Petrogenesis of Lamprophyre from the Giant Weishan REE Deposit in China. Minerals 12(6), 706. https://doi.org/10.3390/min12060706

Taghadosi H. and Malekzadeh Shafaroudi A., 2018. Mineralogy, Alteration, geochemistry, and fluid inclusion studies of Fe oxide-copper mineralization of Namegh area, NE Kashmar.- Iranian Journal of Crystallography and Mineralogy 26(3), 541–554. https://doi.org/10.29252/ijcm.26.3.541

Taghadosi H. and Malekzadeh Shafaroudi A., 2018. Evidences of probable porphyry Cu-Au mineralization in Namegh area, Northeast of Kashmar: geology, Alteration, mineralization, geochemistry, and fluids inclusion studies. Scientific Quarterly Journal of Geosciences 27(108), 105-114. https://doi.org/10.22071/gsj.2017.82914.1094

Ternet Y., Guillou Y., Maurizot P., Berthiaux A., Weecksteen G., Hottin A.M., Andreieff P., Ancelin J., Danesfaleh M., Sajedi T., Alavi Naini M., 1980. Geological map of Iran, Khaf, Scale 1:100,000. Geological Survey of Iran, Tehran.

Thirlwall M.F., Smith T.E., Graham A.M., Theodorou N., Hollings P., Davidson J.P., Arculus R.J., 1994. High field strength element anomalies in arc lavas: source or process?. Journal of Petrology 35(3), 819-838. https://doi.org/10.1093/petrology/35.3.819

Tindell T., Watanabe K., Imai A., Takahashi R., Boyce A.J., Yonezu K., Ogata T., 2018. The Kago low-sulfidation gold and silver deposit: A peripheral mineralisation to the Nansatsu high-sulfidation system, southern Kyushu, Japan. Ore Geology Reviews 102, 951-966. https://doi.org/10.1016/j.oregeorev.2017.10.027

Veloso A.S.R., Monteiro L.V.S., Juliani C., 2020. The link between hydrothermal nickel mineralization and an iron oxide-copper–gold (IOCG) system: Constraints based on mineral chemistry in the Jatobá deposit, Carajás Province. Ore Geology Reviews 121, 103555. https://doi.org/10.1016/j.oregeorev.2020.103555

Verdugo-Ihl M.R., Ciobanu C.L., Cook N.J., Ehrig K.J., Courtney-Davies L., 2020. Defining early stages of IOCG systems: evidence from iron oxides in the outer shell of the Olympic Dam deposit, South Australia. Mineralium Deposita 55, 429-452. https://doi.org/10.1007/s00126-019-00896-2

Walker R. and Mastalerz M., 2004. Functional group and individual maceral chemistry of high volatile bituminous coals from southern Indiana: controls on coking. International Journal of Coal Geology 58(3), 181-191. https://doi.org/10.1016/j.coal.2003.10.008

Westhues A., Hanchar J.M., Voisey C.R., Whitehouse M.J., Rossman G.R., Wirth R., 2017b. Tracing the fluid evolution of the Kiruna iron oxide apatite deposits using zircon, monazite, and whole rock trace elements and isotopic studies. Chemical Geology 466, 303-322. https://doi.org/10.1016/j.chemgeo.2017.06.020

Westhues A., Hanchar J.M., Whitehouse M.J., Martinsson O., 2016. New constraints on the timing of host-rock emplacement, hydrothermal alteration, and iron oxide-apatite mineralization in the Kiruna district, Norrbotten, Sweden. Economic Geology 111(7), 1595-1618. https://doi.org/10.2113/econgeo.111.7.1595

Wilkinson J.J., 2001. Fluid inclusions in hydrothermal ore deposits. Lithos 55(1-4), 229-272. https://doi.org/10.1016/S0024-4937(00)00047-5

Williams P.J., 1998. An introduction to the metallogeny of the McArthur River-Mount Isa-Cloncurry minerals province. Economic Geology 93(8), 1120-1131. https://doi.org/10.2113/gsecongeo.93.8.1120

Williams P.J., Barton M.D., Johnson D.A., Fontboté L, De Haller A., Mark G., Marschik R., 2005. Iron oxide copper-gold deposits: Geology, space-time distribution, and possible modes of origin. https://doi.org/10.5382/AV100.13

WILLIAMS P.J. and POLLARD P.J., 2001. Australian Proterozoic iron oxide-Cu-Au deposits: An overview with new metallogenic and exploration data from the Cloncurry district, northwest Queensland. Exploration and Mining Geology 10(3), 191-213. https://doi.org/10.2113/0100191

Wood D.A., 1979. A variably veined suboceanic upper mantle—genetic significance for mid-ocean ridge basalts from geochemical evidence. Geology 7(10), 499-503. https://doi.org/10.1130/0091-7613(1979)7%3C499:AVVSUM%3E2.0.CO;2

Xavier R.P., Monteiro L.V.S., Souza Filho C.D., Torresi I., Carvalho E.D.R., Dreher A.M., Moreto C.P.N., 2011. The Iron Oxide Copper-Gold Deposits of the Carajás Mineral Province, Brazil. In Hydrothermal iron oxide copper-gold & related deposits: a global perspective; vol. 2 (pp. 285-306). Porter GeoConsultancy PTY.

Xing Y., Etschmann B., Liu W., Mei Y., Shvarov Y., Testemale D., Brugger J., 2019. The role of fluorine in hydrothermal mobilization and transportation of Fe, U and REE and the formation of IOCG deposits. Chemical Geology 504, 158-176. https://doi.org/10.1016/j.chemgeo.2018.11.008

Xu Z., Dilek Y., Cao H., Yang J., Robinson P., Ma C., Chen X., 2015. Paleo-Tethyan evolution of Tibet as recorded in the East Cimmerides and West Cathaysides. Journal of Asian Earth Sciences 105, 320-337. https://doi.org/10.1016/j.jseaes.2015.01.021

Yang G., Li Y., Santosh M., Yang B., Yan J., Zhang B., Tong L., 2012. Geochronology and geochemistry of basaltic rocks from the Sartuohai ophiolitic mélange, NW China: Implications for a Devonian mantle plume within the Junggar Ocean. Journal of Asian Earth Sciences 59, 141-155. https://doi.org/10.1016/j.jseaes.2012.07.020

Yang X., Sun W., Zhou T., Deng J., 2011. The Middle–Lower Yangtze metallogenic belt. International Geology Review 53(5-6), 447-448. https://doi.org/10.1080/00206814.2010.534599

Yousefi L., Haidarian Shahri M.R., Karimpour M.H., 2008. Geology, mineralogy, fluid inclusion thermometry and ground magnetic of Shahrak Magnetite-Specularite Cu-Au prospecting area, Torbat-eHeydariyeh, Iran. Iranian Journal of Crystallography and Mineralogy 16(3), 505-516.

Zhai Q.G., Jahn B.M., Wang J., Hu P.Y., Chung S.L., Lee H.Y., Tang Y., 2016. Oldest paleo-Tethyan ophiolitic mélange in the Tibetan Plateau. Bulletin 128(3-4), 355-373. https://doi.org/10.1130/B31296.1

Zhu Z., 2016. Gold in iron oxide copper–gold deposits. Ore Geology Reviews 72, 37–42. https://doi.org/10.1016/j.oregeorev.2015.07.001

FIGURE CAPTIONS

Figure 1. Simplified structural map of eastern Iran modified from Ramezani and Tucker (2003). showing the location of the Fathabad deposit at the southeastern edge of Dorouneh Fault. Abbreviations: AZF: Abiz fault; BDF: Bahabad fault; BKF: Biabanak fault; CHF: Chap-e-doni fault; DRF: Dorouneh fault; GWF: Gowk fault; KBF: Kuhbanan fault; KMF: Kalmard fault; MAF: Mehdi Abad fault; MBF: Minab fault; NAF: Nosrat Abad fault; NHF: Nehbandan fault; NNF: Naein fault; RJF: Rafsanjan fault; SBF: Shahr-e-Babak fault; TKF: Teknar fault; UZF: Uzbakkuh fault; ZRF: Zarand fault; ZTZ: Zagros thrust zone.

Figure 2. The Fathabad deposit is part of the Khaf-Kashmar-Bardaskan volcano-plutonic belt (KKBVPB). The location of this belt has been shown in northeastern Iran (Geological Survey of Iran, 2002)

Figure 3. The simplified geological map of northeastern Roshtkhar and location of the Fathabad district (black star), (modified after the 1:100000 geological map of Roshtkhar (Ternet et al., 1980) and 1:100000 map of Dolatabad (Kholghi-Khasraghi et al., 1996).

Figure 4. Simplified geological map of Fathabad deposit.

Figure 5. a) Stratigraphic sequences of the central part of the study area, microdiorite unit between granite and Eocene volcanics, b) dark grey megaporphyitic andesite with plagioclase

macrocrysts and dark sandy tuff, c) light grey megaporphyitic andesite with plagioclase megacrysts showing sericitic and argillic alteration, d) tectonic orientation in the agglomerate unit.

Figure 6. Photomicrograph of the different types of alteration in the Fathabad deposit. a) propylitic alteration in light grey andesite unit, b) propylitic alteration zone (green) adjacent to argillic zone (light brown) with oxidized sulfide veins, c-d) NE-SW - quartz vein with sulfide and oxide minerals, e) quartz vein in granite intrusive unit with argillic and hematite, f) quartz, feldspar, potassium, plagioclase and biotite in granite unit.

Figure 7. Photo and micrograph of the different types of alteration in the Fathabad deposit: a) calcite in the center of the vein and quartz in the vein walls, b) opaque crystals in the center of the quartz veins with sericitic alteration, c) a form of ferromagnesian (pyroxene) replaced by opaque minerals at the margin and centrally by epidote, sericitized and argillic plagioclase with opaque minerals in porphyritic andesite, d) sericitic and argillic alteration of plagioclase and hornblende crystal against a background of scattered epidote crystals and opaque minerals. Abbreviations: calcite (Cal), epidote (Ep), hornblende (Hb), opaque minerals (Opq), plagioclase (Pl), pyroxene (Px), quartz (Qtz), sericite (Ser).

Figure 8. Photomicrograph of, a) view of an approximately 1.5 m thick quartz vein of copper mineralization in andesitic rock, b) veins of copper and iron oxide mineralization in the fracture of the porphyritic andesite unit, c) agglomerate block with silica fragments and copper oxide mineralization, d) sulfide minerals (pyrite, chalcopyrite, chalcocite) and oxide minerals (malachite and iron oxides) as open space fillings of the quartz veins. e) adjacent to pyrite and chalcopyrite, chalcopyrite is replaced by covellite from the edge, f) replacement of chalcocite and bornite by chalcopyrite, subhedral chalcopyrite crystals are internally oxidised to Fe oxides. Abbreviations: bornite (Bn), chalcopyrite (Ccp), chalcocite (Cct), covellite (Cv), goethite (Geo), hematite (Hm), limonite (Lim), magnetite (Mt), malachite (Mal), pyrite (Py).

Figure 9. Paragenetic sequence of the Fathabad deposits.

Figure 10. Photomicrographs of ore minerals under reflected light (PPL): a) alteration of chalcopyrite from rim to covellite, b) euhedral to subhedral magnetite crystals, c) inclusions of hematite, limonite and goethite, magnetite slightly replaced by hematite, d) magnetite, hematite and goethite. Abbreviations: bornite (Bn), chalcopyrite (Ccp), chalcocite (Cct), covellite (Cv), goethite (Geo), hematite (Hm), limonite (Lim), magnetite (Mt), malachite (Mal), pyrite (Py).

Figure 11. Classification of Fathabad volcanic rocks by plotting, a) total alkali vs. silica diagram after (Le Maitre, 2002), b) SiO_2 vs. K_2O, separating shoshonitic magmas from high-K, calc-alkaline magmas after Peccerillo and Taylor (1976), c) A/NK (molar Al_2O_3/Na_2O+K_2O) vs. A/CNK (molar $Al_2O_3/CaO+Na_2O+K_2O$) diagram after Maniar and Piccoli (1989).

Figure 12. Plots of various major oxides and trace elements versus SiO_2 for volcanic rocks from the study area: a) Fe_2O_3, b) MgO, c) CaO, d) Al_2O_3, d) TiO_2, e) P_2O_5, f) Co, g) Sr, h) Eu*, i) Fe_2O_3 vs. MgO diagram. Symbols are the same as in Figure 11.

https://doi.org/10.5281/zenodo.15130089

Figure 13. Whole rock primitive mantle normalized, a) rare earth element (REE) patterns and b) trace element patterns for volcanic rocks from the Fathabad deposit. (Primitive mantle values are from Sun and McDonough (1989).

Figure 14. Micrograph of FIs in quartz and calcite minerals from the Fathabad deposit: a) primary two-phase (LH_2O+V) FIs, with 80 vol% liquid, b) primary monophase liquid FIs (L) and two-phase (LH_2O+V) FIs. liquid (L), vapor (V).

Figure 15. Histograms of final homogenization temperatures (Th) and salinities (% NaCl equiv.) for all inclusion types in different host minerals and stages, in the Fathabad deposit.

Figure 16. Geochemical classification diagrams for the Fathabad volcanic rocks on, a) Sr/Y vs.Y diagram, b) $(La/Yb)_N$ vs.Yb_N diagram from Defant and Drummond (1990). Symbols are the same as in Figure 11.

Figure 17. Plot of Fathabad volcanic rock samples on, a) La/Yb vs. La diagram. Partial melting (PM) vector is from Thirlwall et al. (1994), b) Sm/Yb vs. La/Sm diagram from Aldanmaz et al. (2000), c) $(La/Yb)_N$ vs. $(Dy/Yb)_N$ diagram; crystal fractionation trend line for garnet and amphibole from He et al. (2011). Symbols are the same as in Figure 11.

Figure 18. Discrimination diagrams for the volcanic rocks of the Fathabad deposit: a) Yb vs. Th/Ta diagram (Gorton and Shandl, 2000), b) La/Yb vs. Th/Nb diagram (Hollocher et al., 2012), c) Rb and Y+Nb discrimination diagram (Forster et al., 1997; Pearce et al., 1984), d) Hf/3-Th-Nb/16 triangular diagram showing the affinity of continental volcanic arc basalts from samples (Wood, 1979). Abbreviations: within-plate related (WIP), island-arc tholeiite (IAT), island-arc calc-alkaline basalt (CAB), normal mid-oceanic ridge basalt (N-MORB), enriched mid-oceanic ridge basalt (E-MORB); within-plate alkaline basalt (WPA), volcanic rocks mainly consistent with calc-alkaline basalt to shoshonitic basalt (CAB) and within-plate basalts (WPB), e) Ta/Yb vs. Th/Yb diagram modified from Pearce (1983). Symbols are the same as in Figure 11.

Figure 19. Homogenization temperature versus salinity of mineralizing fluid inclusions in quartz and calcite veins of the Fathabad deposit. Possible trends of fluid evolution in temperature-salinity diagram (Wilkinson, 2001), dotted lines of pressure curves (Ramdohr, 1980) and black lines of density curves (Brown and Lamb, 1988).

TABLES

Appendix Table 1. X-ray diffraction (XRD) data.

Sample	Major phase	Minor phase
FA46	Albite+ Quartz	Calcite+ Illite+ Muscovite
FA008	Quartz+Albite+ Calcite	Muscovite+ Illite
FA11	Quartz+Albite+ Muscovite	Orthoclase
FA007	Quartz+Orthoclase+Albite+ Muscovite	_
FA051	Quartz+Calcite+Albite+ Orthoclase	Muscovite
FA049	Orthoclase+Quartz+Calcite+Albite+ Magnetit+Muscovite	_
FA066	Orthoclase+ Quartz+ Albite	Illite+ Muscovite

https://doi.org/10.5281/zenodo.15130089

FA060	Albite+ Quartz	Montmorillonite-Cholorite

Appendix Ttable 2. Major, trace, and REE elements analysis of least–altered volcanic rocks from the Fathabad deposit.

		FA012	FA011	FA010	FA009	FA008	FA007	FA006	FA005	FA004	FA003	FA002	FA001
	Detection Limit	Basaltic-trachyandesite			Trachybasalt			Trachyandesite		Trachyte, Trachydacite	Rhyolite		
SiO_2 (wt.%)		50	49	51	50	47	51	55	58	67	69	72	74
Al_2O_3		15	19	16	14	18	17	19	17	15	15	14	13
CaO		9.4	7.8	7.8	8.5	6.3	7.8	4	3	2.9	1.8	1.2	0.9
MgO		2.2	1.1	5.1	7.3	4.2	6.1	2	1.7	1.3	0.4	0.2	0.2
TiO_2		1	0.6	1.2	1	0.8	0.9	0.7	0.8	0.4	0.8	0.8	0.8
Fe_2O_3		7.9	6.4	9.2	9.3	9.7	5.2	6.2	7.3	3.5	2.4	1.6	1.5
MnO		0.2	0.2	0.8	0.8	0.2	0.8	0.8	0.8	0.8	0.8	0.8	0.8
P_2O_5		0.8	0.5	1.1	0.9	0.4	0.4	0.6	0.5	0.2	0.3	0.1	0.1
Na_2O		3.6	2.8	3.3	3	4.1	5	3.8	4.4	3.5	3.8	3.3	3.4
K_2O		3.9	5.5	3	2.9	1.5	0.7	5.7	3.5	5.1	5.6	5.7	5.9
L.O.I		6	6.3	1.8	2.4	7.4	5.6	2	3.4	0.9	1.4	1.2	0.9
TOTAL		99	100	100	100	100	100	100	101	101	101	101	101
La	1 ppm	22	12	38	37	9.8	3.9	8.5	7	4.5	11	10	23
Ce	0.5 ppm	46	27	74	70	24	12	19	20	10	24	23	40
Pr	0.05 ppm	5.2	3	8.2	7.6	2.7	1.4	2.2	2.2	1.2	2.8	2.7	4.5
Nd	0.5 ppm	20	11	31	28	11	6.5	8.5	9.2	4.4	9.9	9.7	14
Sm	0.02 ppm	4	2.3	5.4	5	2.7	2	1.9	2.1	1	1.9	2.2	2.5
Eu	0.1 ppm	1.6	0.7	1.2	1.2	0.9	0.7	0.5	0.5	0.2	0.3	0.2	0.2
Gd	0.05 ppm	3.3	2	4.5	4.3	2.8	2.2	1.6	2.1	1.1	1.5	2	2.2
Tb	0.1 ppm	0.4	0.3	0.6	0.6	0.4	0.4	0.2	0.3	0.2	0.2	0.3	0.3
Dy	0.02 ppm	2.4	1.5	3.3	3.1	2.7	2.3	1.3	2	1.2	1	2	2.1
Ho		0.5	0.3	0.6	0.6	0.5	0.5	0.2	0.4	0.3	0.2	0.4	0.4
Er	0.05 ppm	0.7	0.4	1	1	0.8	0.7	0.4	0.6	0.4	0.3	0.6	0.6
Tm	0.1 ppm	0.2	0.1	0.2	0.2	0.2	0.2	0.1	0.2	0.1	0.1	0.2	0.2
Yb	0.05 ppm	0.7	0.4	0.9	0.9	0.8	0.7	0.3	0.6	0.5	0.2	0.6	0.7
Y	0.5 ppm	9.8	5.5	15	14	11	10	4.4	6.9	5.2	3	7.3	9.9
Hf	0.5 ppm	0.8	1.9	2.5	3.1	0.8	0.9	1	1	0.3	0.2	0.3	0.5
Th	0.1 ppm	4.4	3.1	5.4	7.5	1	0.7	2.1	1.2	3.5	5.6	7.4	22
Ta	0.1 ppm	0.8	0.9	1.6	1.4	0.5	0.4	0.9	0.6	0.8	0.6	0.9	1.2
Ga		11	15	17	16	16	12	15	16	11	12	13	12
Cs	0.5 ppm	0.5	2.2	0.5	0.6	1.2	0.6	0.8	0.6	3.5	2.1	1.3	2.2
Cr	1 ppm	103	63	116	156	67	67	65	62	66	81	87	63
Li	1 ppm	16	5.9	11	16	21	27	14	15	22	5	5.7	5.6
Be	0.2 ppm	0.6	1.5	1.8	1.5	0.8	1.3	1.5	0.7	0.7	0.5	1	1.6
Nb	1 ppm	24	29	48	44	14	10	30	15	17	20	21	19
Rb	1 ppm	23	22	17	38	14	8.2	12	26	20	46	45	110
Sr	1 ppm	265	218	627	557	137	466	704	145	132	94	67	45
Zr	5 ppm	38	81	135	185	20	50	45	34	6.8	5.8	9.6	14
Ba	1 ppm	556	469	537	454	33	116	714	346	268	332	196	85
Sn	0.1 ppm	6.4	3.7	4.4	7.3	1.8	1.7	2.2	2.3	18	4	5.6	13
Co	1 ppm	13	9	25	26	16	18	12	7.6	7.2	2.3	2.4	2.1
Sc	0.5 ppm	6.5	2.3	11	11	10	13	2.1	3.3	2.3	0.8	2.4	1.3
W	1 ppm	1.8	1.2	1.5	2.2	2.1	0.8	1.2	4.5	2.4	1.7	0.9	1.9

https://doi.org/10.5281/zenodo.15130089

V	1 ppm	125	72	145	148	167	156	88	38	43	10	6.3	6
U	0.1 ppm	1.1	1.1	1.2	1.8	0.3	0.3	0.8	0.3	2.4	1.9	1.8	3.3
Ni	1 ppm	35	11	45	85	8	48	11	5.7	8.4	7.1	7.1	7.6
Mn	5 ppm	1196	925	1009	887	826	714	293	431	444	522	90	136
Pb	1 ppm	84	29	16	170	16	17	26	16	41	55	62	91
Zn	1 ppm	307	64	126	105	68	185	72	74	86	107	63	88
Mo	0.1 ppm	1	2.8	3.4	1.2	0.9	1.2	1.6	1	2	2.3	1.8	1.8
Cu	1 ppm	1258	281	4.7	679	1	3.5	4.8	4.4	66	42	19	29
As (ppm)	0.1 ppm	6.4	5.5	6.9	7.3	6.2	6.1	7.6	6.4	7	6	19	5.9
Au (ppb)		190	199	187	15.25	580	251	678	617	10	-	3021	1313
Sr/Y		27	39	43	40	13	45	161	21	25	31	9.1	4.5
Eu/Eu$_N$		1.4	0.97	0.74	0.77	0.97	1.06	0.95	0.77	0.61	0.51	0.28	0.19
(La/Yb)$_N$		23.7	20	29.4	31.2	8.75	3.99	17.8	8.36	7.02	37.6	11.9	23.3
(Dy/Yb)$_N$		2.48	2.2	2.4	2.4	2.24	2.16	2.56	2.19	1.73	3.19	2.11	1.92
(Sm/Yb)$_N$		6.8	5.73	6.45	6.56	3.68	3.2	6.04	3.83	2.51	9.99	3.79	3.92

Appendix Table 3. Summary of microthermometric data from the primary Two-phase (LH2O+vapour) FIs of the quartz and calcite minerals from the Fathabad Cu±Au deposit.

Notes 1. Te (Ice): eutectic temperature; Tm(Ice): final ice melting temperature; Th: homogenization temperature. The salinities of H_2O- NaCl+$CaCl_2$ systems were calculated using the ice points (Tm(ice); after Bodnar (1993). Density in the H_2O-NaCl+$Cacl_2$ system after Flincor software Brown (1989).

Host mineral	FI Number	Size (µm)	Type	Origin	Te / °C	Tm(ice) / °C	Salinity wt% NaCl+CaCl2	Th (°C) Min/Ave/Max	Density /g/cm3
Quartz	115	4 to 35	LV	Primary	−41 to −52	−8.4 to −24.7	12.30 to 23.83	85/150/ 210	0.99 to 1.16
Calcite	16	4 to 12	LV	Primary	−41 to −52	−14 to −21	17.33 to 23.05	135/160/208	1.03 to 1.10

Appendix Table 4. Fathabad gold copper deposits and some epithermal deposits in Iran.

Main feature	Fathabad Deposite	Khalifehlu deposit	Goluje epithermal deposit	cheshmeh Noghreh
Base metals	Cu- Au	Cu- Au	Base metals	Cu- Au
geographical location	Fathabad-Roshtkhar	Tarom,North of Khoramdareh	North of Zanjan	Southwest of Kashmar
structural zone	Khaf- Dorouneh	Tarom magmatic zone	Tarom–Hashtjin	Khaf- Dorouneh
Host Rock	andesite, latite-andesite amygdaloidal and granite	lava and pyroclastic quartz monzonite porphyry	basaltic andesite, andesite and trachy andesite, dacite and tuff	pyroclastic
age of mineralization	Eocene	Eocene	Eocene- Oligocene	Tertiary
Control of mineralization	Joint, fracture, fault	fault	Joint, fracture, fault	fault

Mineralogy	chalcopyrite, galena, pyrite, burnite, covelite	chalcopyrite, bornite, gold, pyrite, Covelite	galena, sphalerite, chalcopyrite and pyrite	pyrite, iron oxides, malachite and azurite
texture and structure	Massive, stripe,Radial, comb, vein-veinlet, shear, scatterd, carbonate substituted	vein-veinlet, Shear, vesicular, massive	Shear, stripe, veinlet, dispersed distribution of mineral grains	dispersed distribution of mineral grains, voids filling, vein-veinlet
Alteration	Quartz, chlorite, epidote, Carbonate and sericite	Quartz, alunite	arjelic, phyllic, and propylitic, silicic	arjelic, propylitic, sericite
type of Mineralization	Epithermal (LS)	Epithermal (HS)	Epithermal (LS)	Epithermal (LS)
Reference	This paper	HOSSEINZADEH et al. (2015)	MEHRABI et al. (2009)	ALAMINIA et al. (2010)

Appendix Table 5. Sulfur isotope values of chalcopyrite in quartz vein.

Sample name	Rock	Sulphide mineral	Quartz vein	$\delta^{34}S$(‰)	$\delta^{34}SH_2S$
BHFA-B35	Porphyritic andesite	Chalchopyrite	Quartz+ Chalchopyrite+pyrite+malachite+Hematite	-1.58	-1.94
BHFA-B12	Porphyritic andesite	Chalchopyrite	Quartz+ Chalchopyrite+pyrite+Chalcocite+malachite+Hematite	-2.86	-3.15

FIGURES

https://doi.org/10.5281/zenodo.15130089

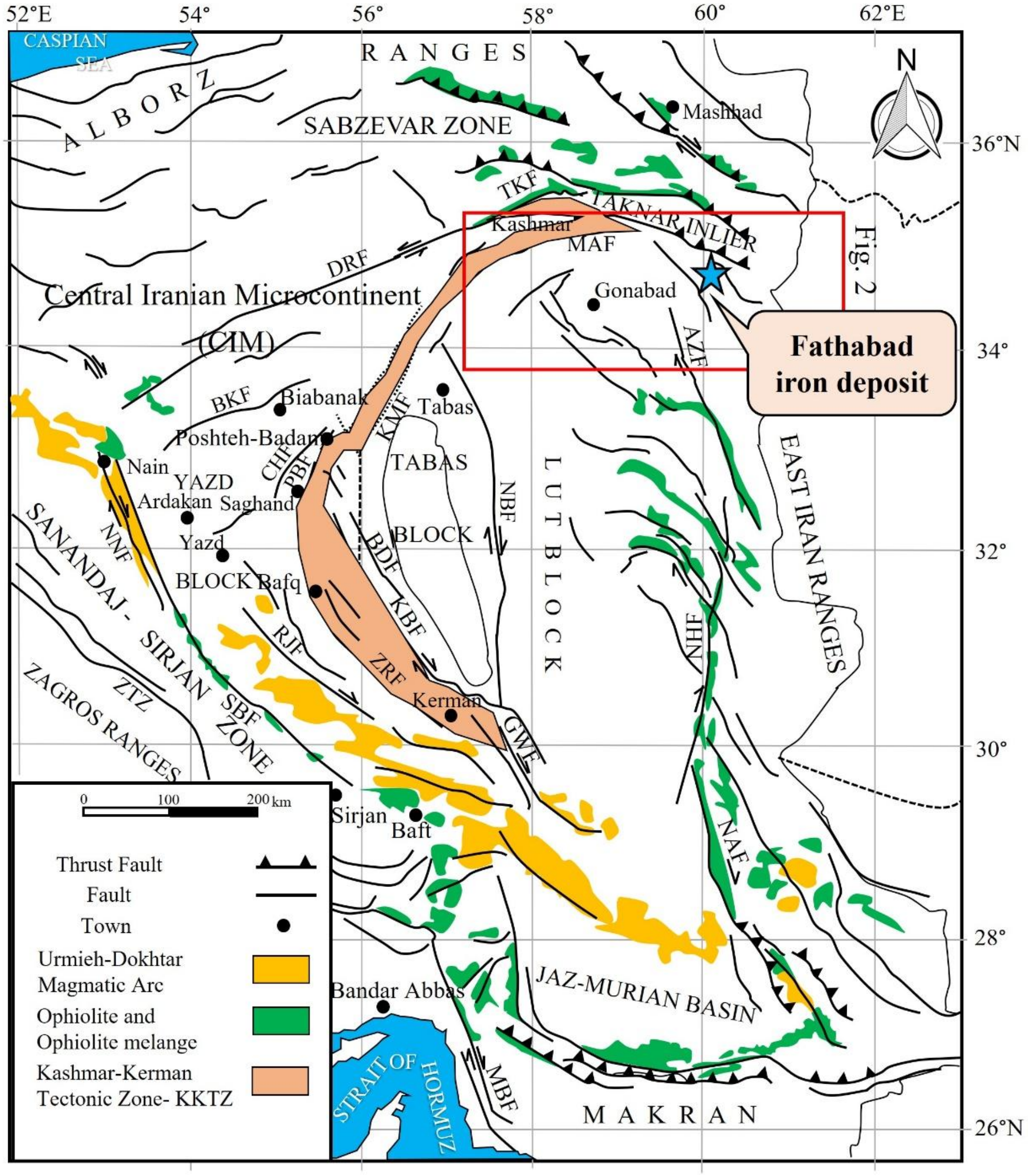

Figure 1

https://doi.org/10.5281/zenodo.15130089

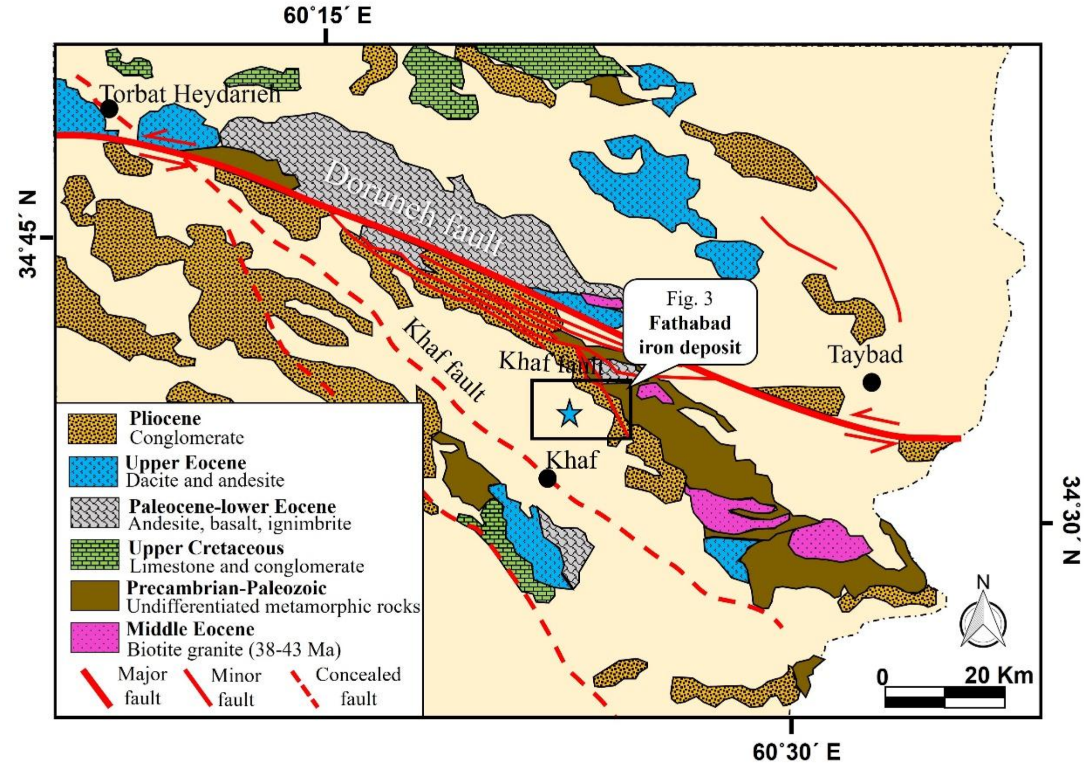
60˚15´ E
34˚45´ N
34˚30´ N
60˚30´ E
Torbat Heydarieh
Doruneh fault
Fig. 3
Fathabad
iron deposit
Taybad
Khaf fault
Khaf fault
Khaf
Pliocene
Conglomerate
Upper Eocene
Dacite and andesite
Paleocene-lower Eocene
Andesite, basalt, ignimbrite
Upper Cretaceous
Limestone and conglomerate
Precambrian-Paleozoic
Undifferentiated metamorphic rocks
Middle Eocene
Biotite granite (38-43 Ma)
Major fault
Minor fault
Concealed fault
N
0
20 Km

Figure 2

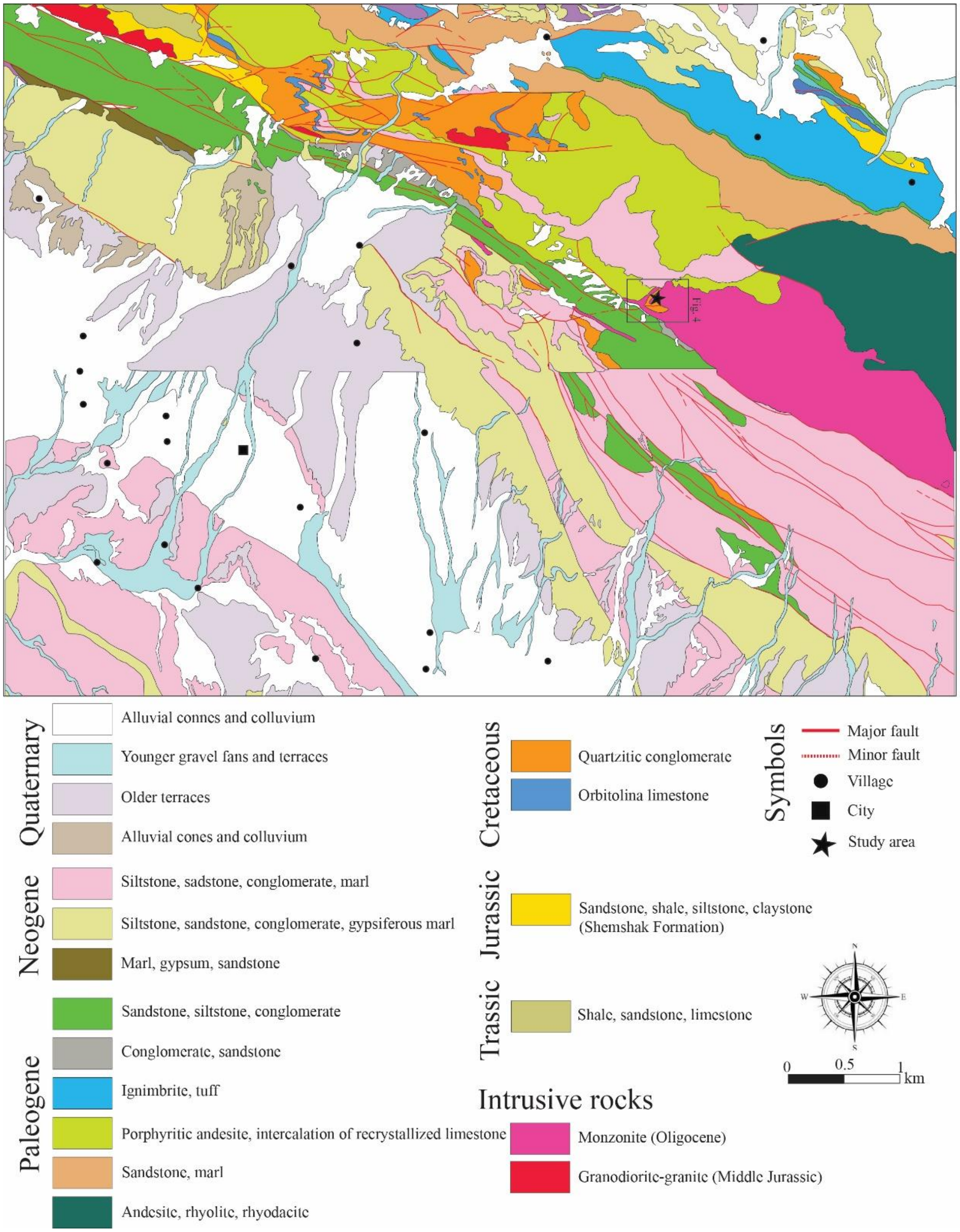
Fig 4
Quaternary
Alluvial connes and colluvium
Younger gravel fans and terraces
Older terraces
Alluvial cones and colluvium
Neogene
Siltstone, sadstone, conglomerate, marl
Siltstone, sandstone, conglomerate, gypsiferous marl
Marl, gypsum, sandstone
Paleogene
Sandstone, siltstone, conglomerate
Conglomerate, sandstone
Ignimbrite, tuff
Porphyritic andesite, intercalation of recrystallized limestone
Sandstone, marl
Andesite, rhyolite, rhyodacite
Cretaceous
Quartzitic conglomerate
Orbitolina limestone
Jurassic
Sandstone, shale, siltstone, claystone (Shemshak Formation)
Trassic
Shale, sandstone, limestone
Intrusive rocks
Monzonite (Oligocene)
Granodiorite-granite (Middle Jurassic)
Symbols
Major fault
Minor fault
Village
City
Study area
N
W
E
S
0
0.5
1
km

Figure 3

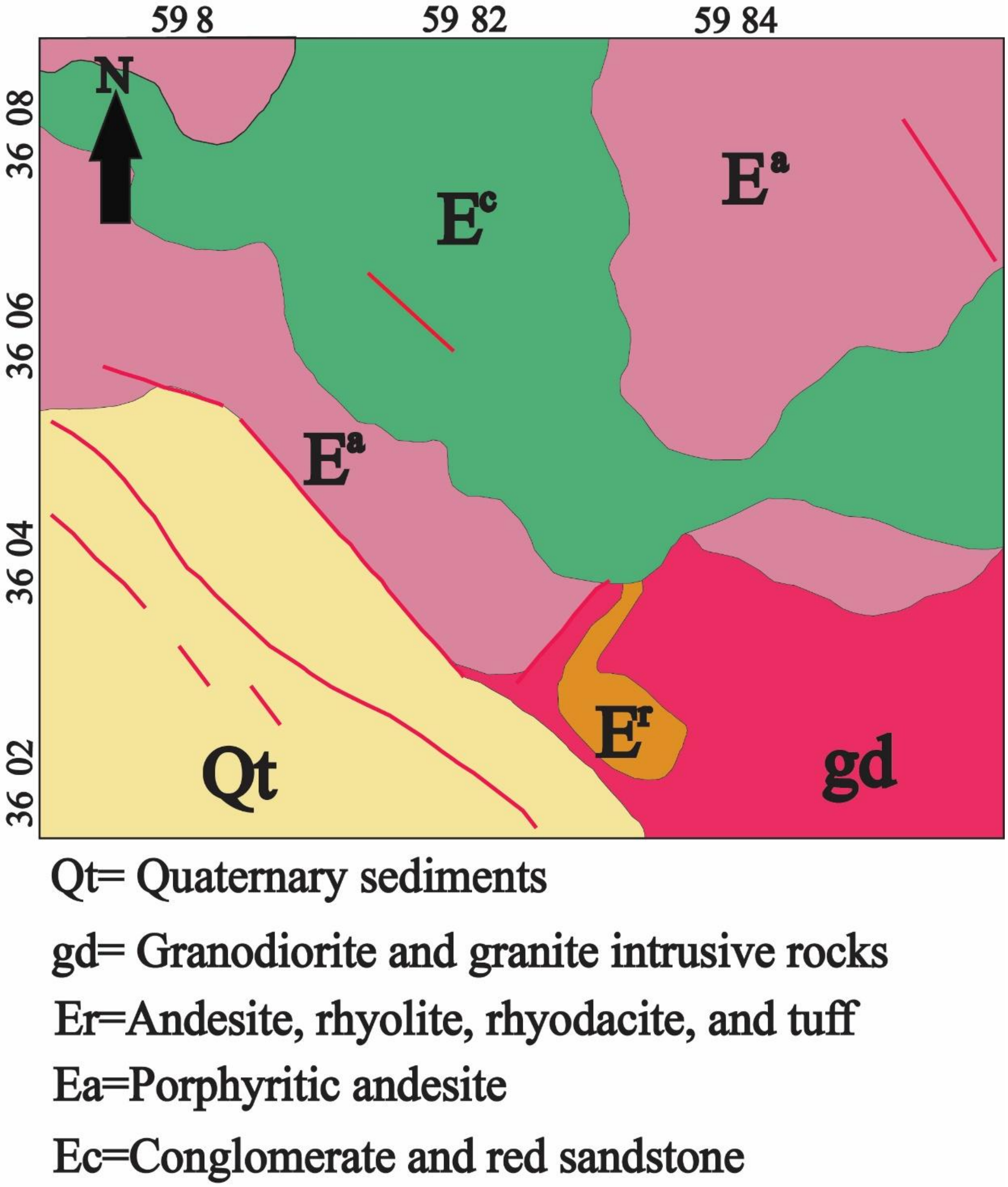
59 8
59 82
59 84
36 08
36 06
36 04
36 02
N
E^c
E^a
E^a
E^r
Qt
gd
Qt= Quaternary sediments
gd= Granodiorite and granite intrusive rocks
Er=Andesite, rhyolite, rhyodacite, and tuff
Ea=Porphyritic andesite
Ec=Conglomerate and red sandstone

Figure 4

Figure 5

https://doi.org/10.5281/zenodo.15130089

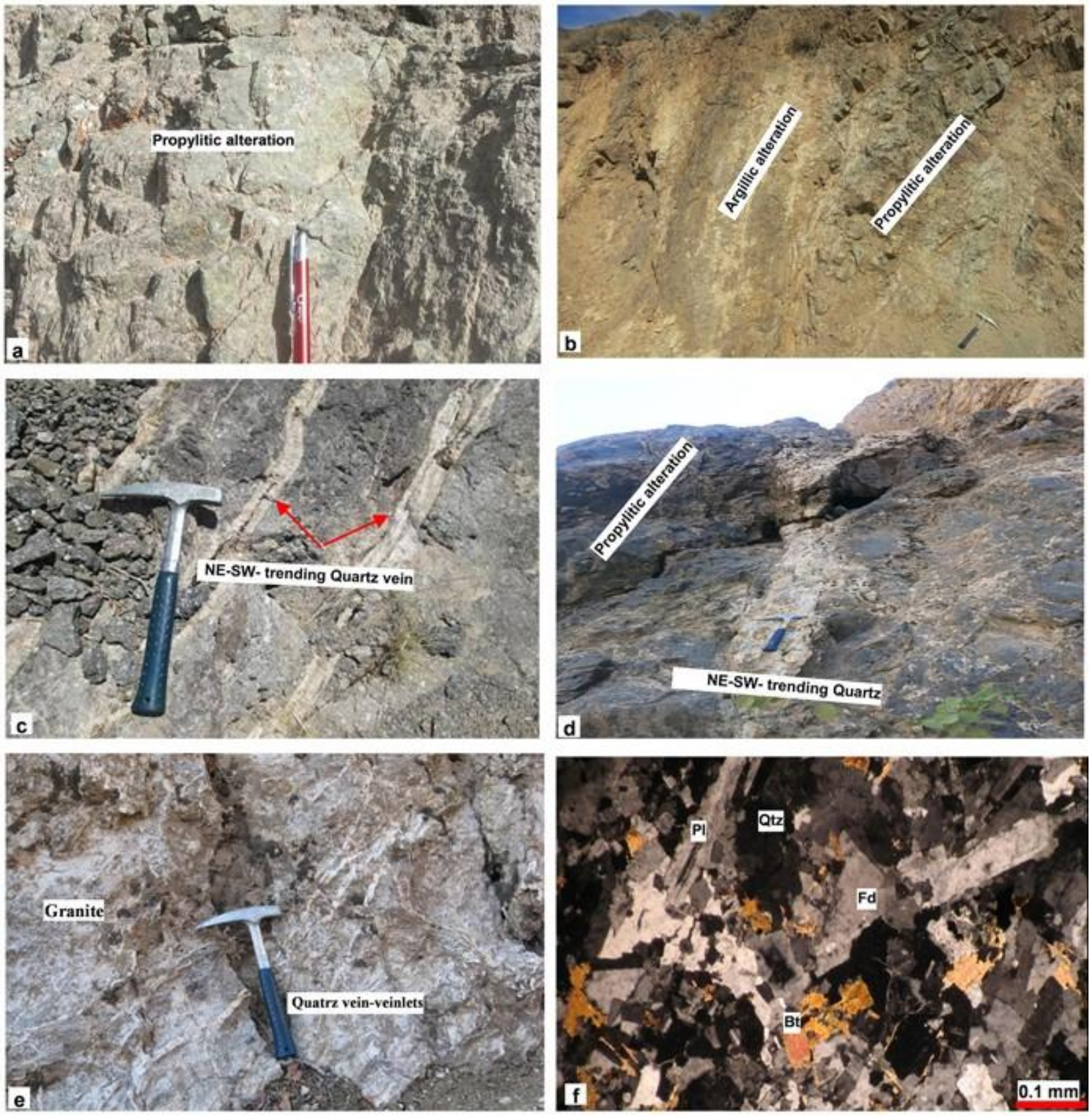
Propylitic alteration
a
Argillic alteration
Propylitic alteration
b
NE-SW- trending Quartz vein
c
Propylitic alteration
NE-SW- trending Quartz
d
Granite
Quatrz vein-veinlets
e
Pl
Qtz
Fd
Bt
0.1 mm
f

Figure 6


Hb
Plg
Qtz
Cal
Hb
Opq
a
0.5 mm
Qtz
Opq
Sericitic alteration
b
0.5 mm
Ser
Pl
Px?
Ep
Opq
Pl
c
0.1 mm
Pl
Hb?
d
0.1 mm

Figure 7

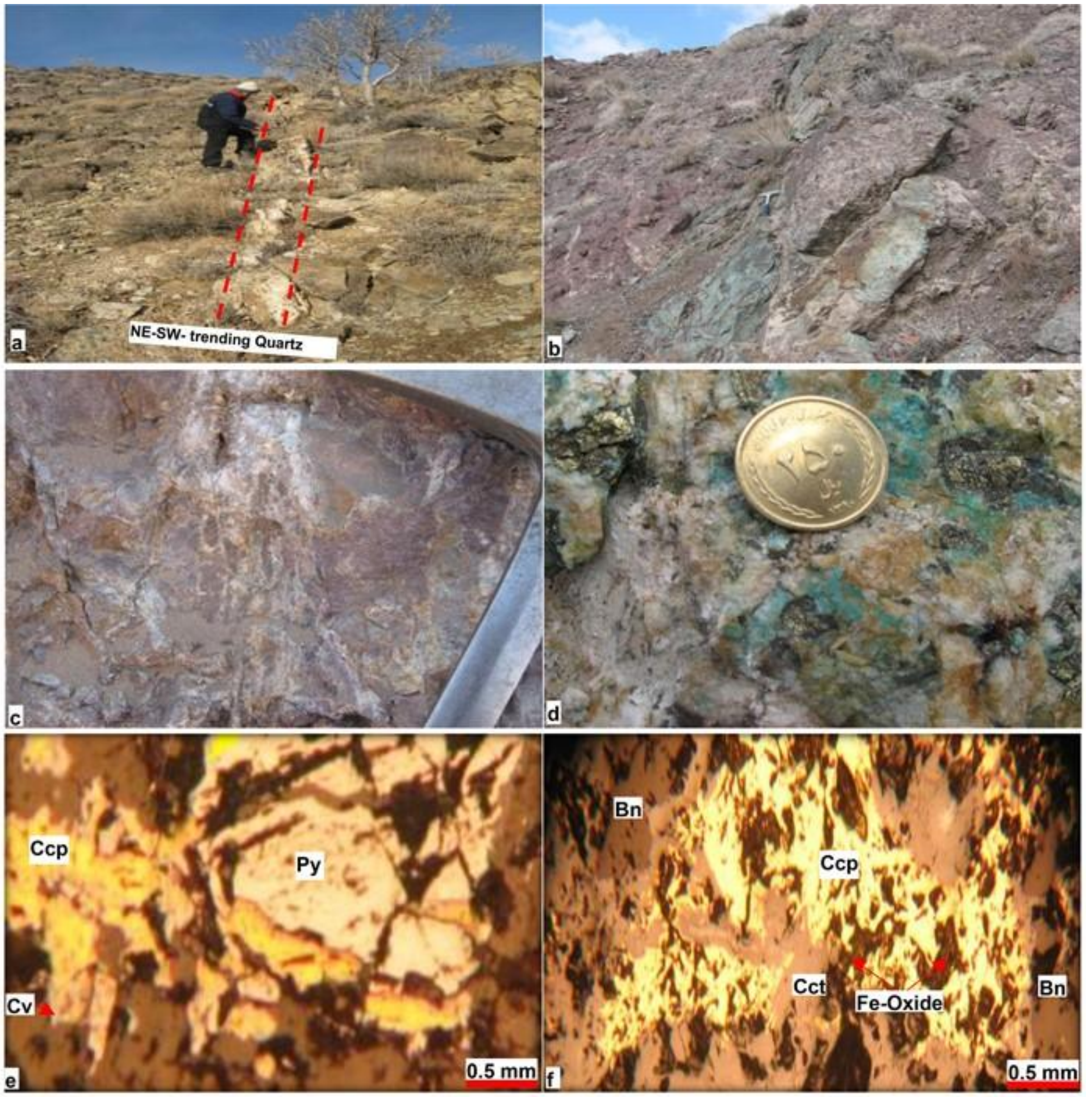
a
NE-SW- trending Quartz
b
c
d
Ccp
Py
Cv
e
0.5 mm
Bn
Ccp
Cct
Fe-Oxide
Bn
f
0.5 mm

Figure 8

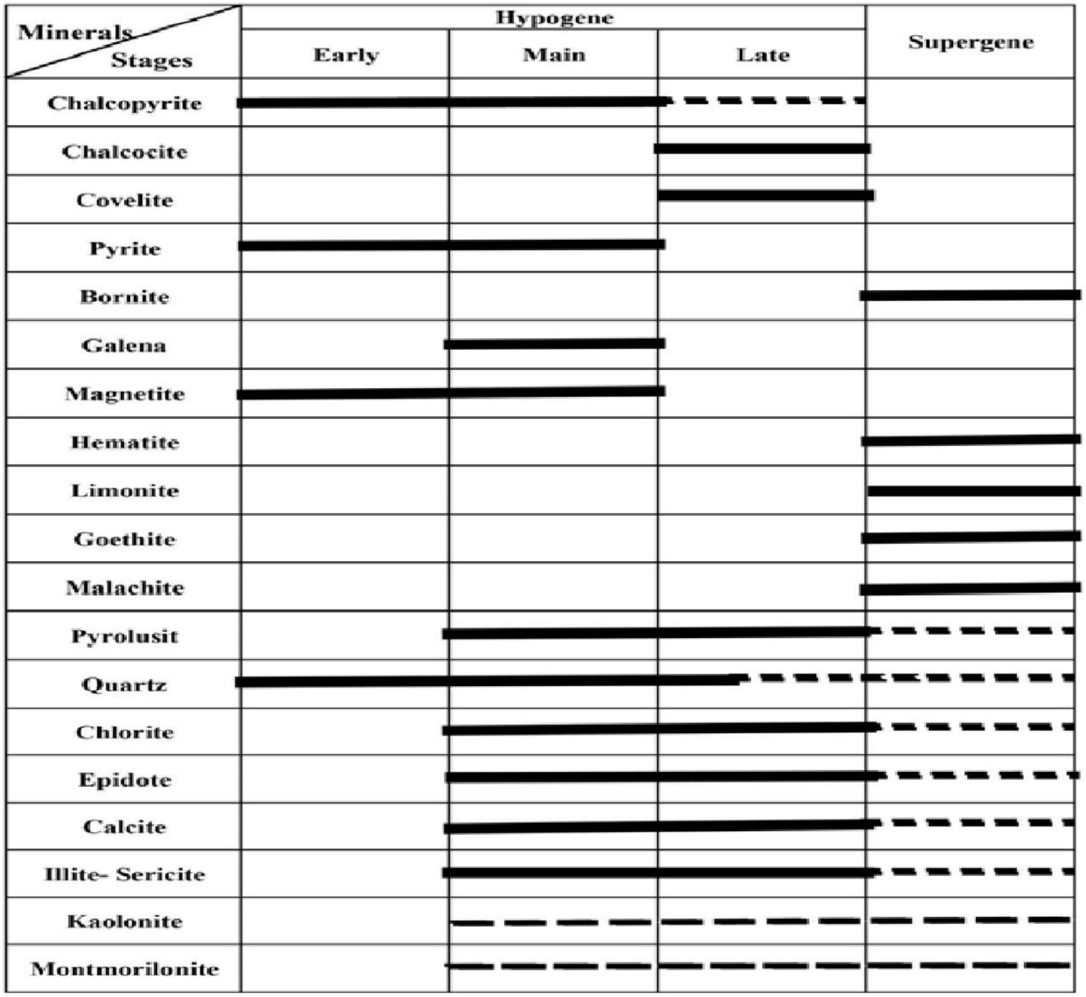
Minerals
Stages
Hypogene
Early
Main
Late
Supergene
Chalcopyrite
Chalcocite
Covelite
Pyrite
Bornite
Galena
Magnetite
Hematite
Limonite
Goethite
Malachite
Pyrolusit
Quartz
Chlorite
Epidote
Calcite
Illite- Sericite
Kaolonite
Montmorilonite

Figure 9

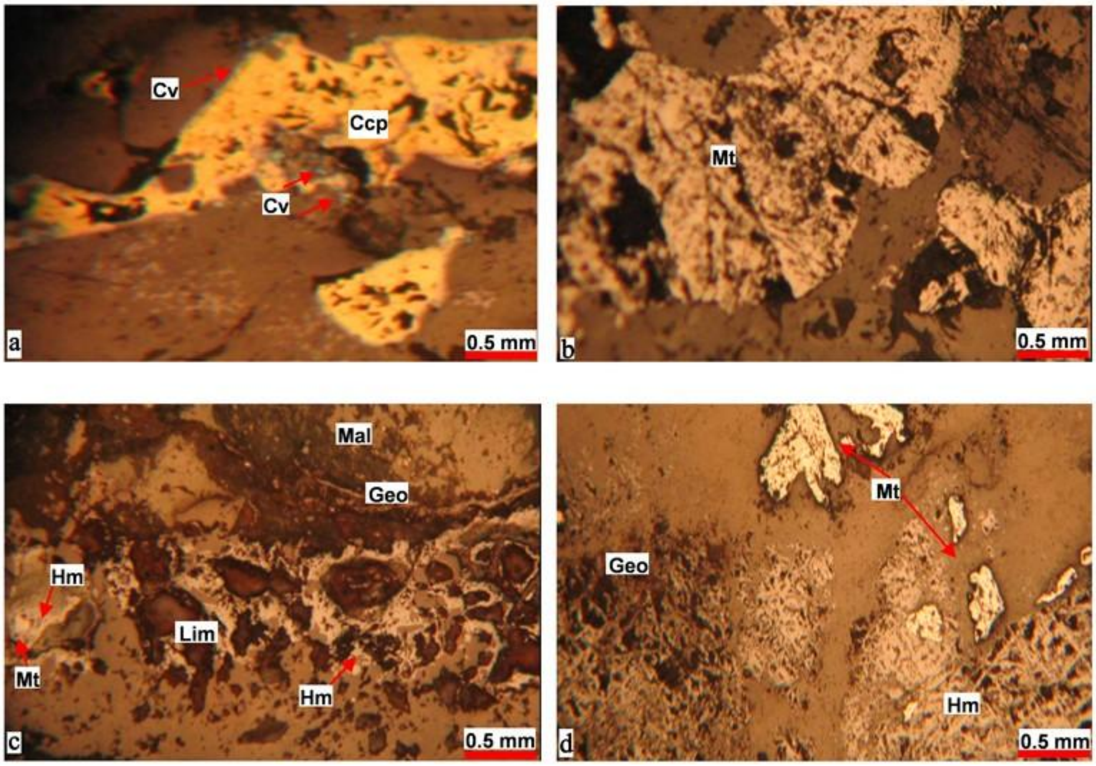
Cv
Ccp
Cv
a
0.5 mm
Mt
b
0.5 mm
Mal
Geo
Hm
Mt
Lim
Hm
c
0.5 mm
Mt
Geo
Hm
d
0.5 mm

Figure 10

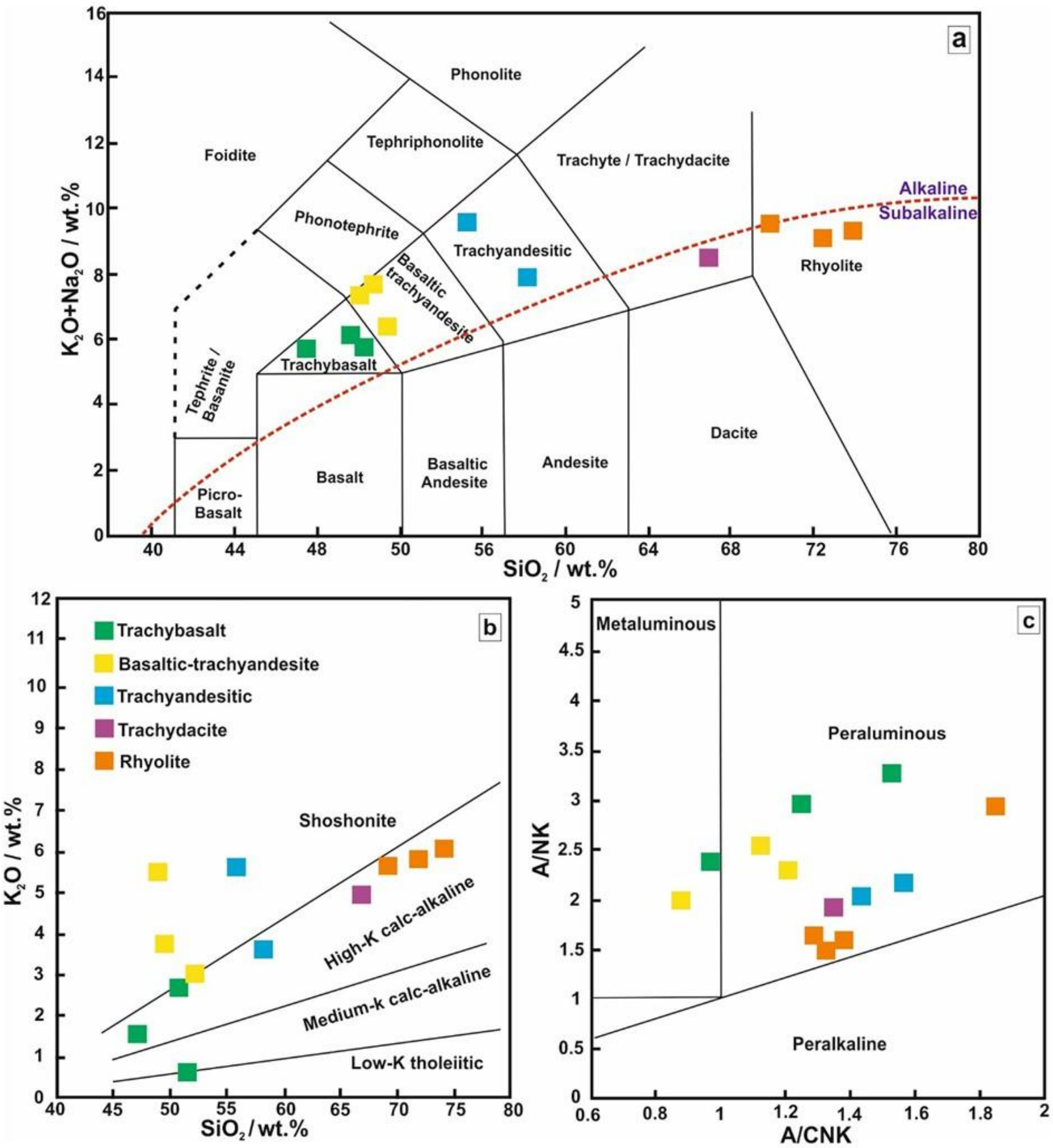

Figure 11

https://doi.org/10.5281/zenodo.15130089

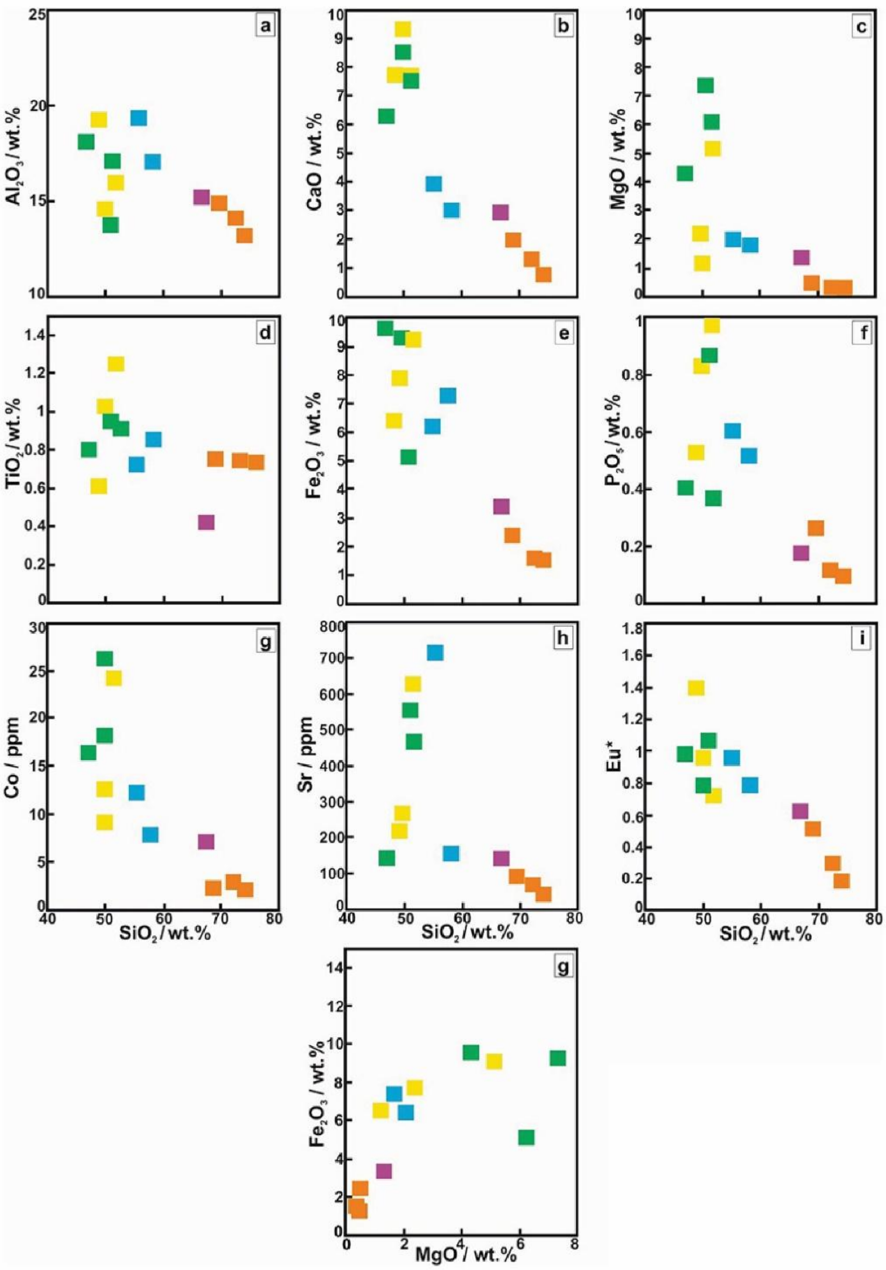
a
Al_2O_3 / wt.%
25
20
15
10
b
CaO / wt.%
c
MgO / wt.%
d
TiO_2 / wt.%
e
Fe_2O_3 / wt.%
f
P_2O_5 / wt.%
g
Co / ppm
h
Sr / ppm
i
Eu*
SiO_2 / wt.%
40
50
60
70
80
g
Fe_2O_3 / wt.%
MgO / wt.%

Figure 12

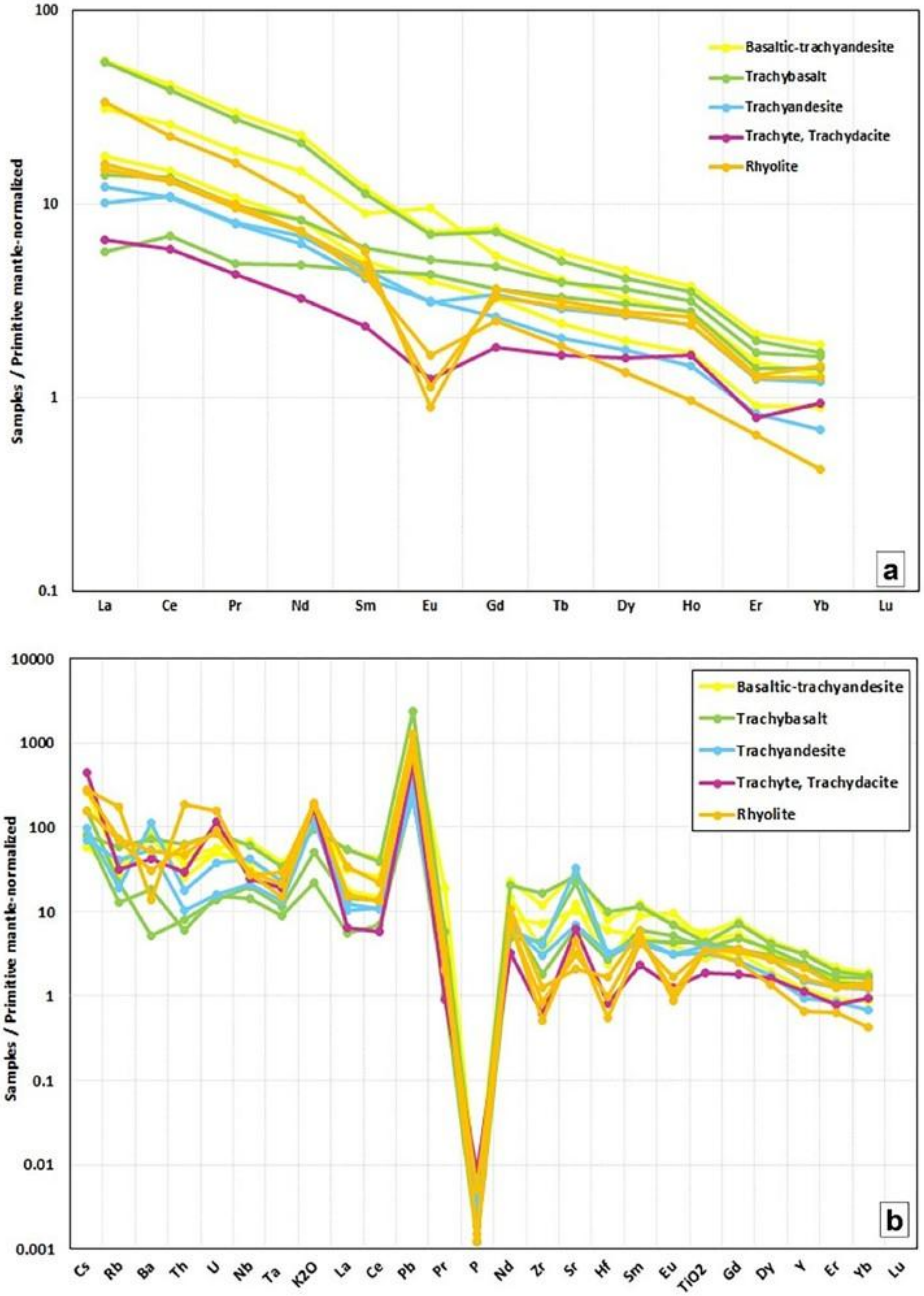
100
10
1
0.1
Samples / Primitive mantle-normalized
Basaltic-trachyandesite
Trachybasalt
Trachyandesite
Trachyte, Trachydacite
Rhyolite
La
Ce
Pr
Nd
Sm
Eu
Gd
Tb
Dy
Ho
Er
Yb
Lu
a
10000
1000
100
10
1
0.1
0.01
0.001
Samples / Primitive mantle-normalized
Basaltic-trachyandesite
Trachybasalt
Trachyandesite
Trachyte, Trachydacite
Rhyolite
Cs
Rb
Ba
Th
U
Nb
Ta
K2O
La
Ce
Pb
Pr
P
Nd
Zr
Sr
Hf
Sm
Eu
TiO2
Gd
Dy
Y
Er
Yb
Lu
b

Figure 13

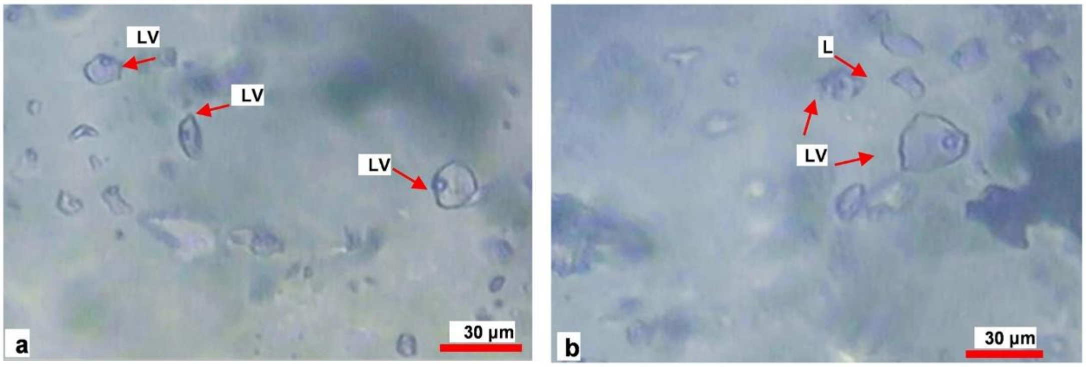

Figure 14

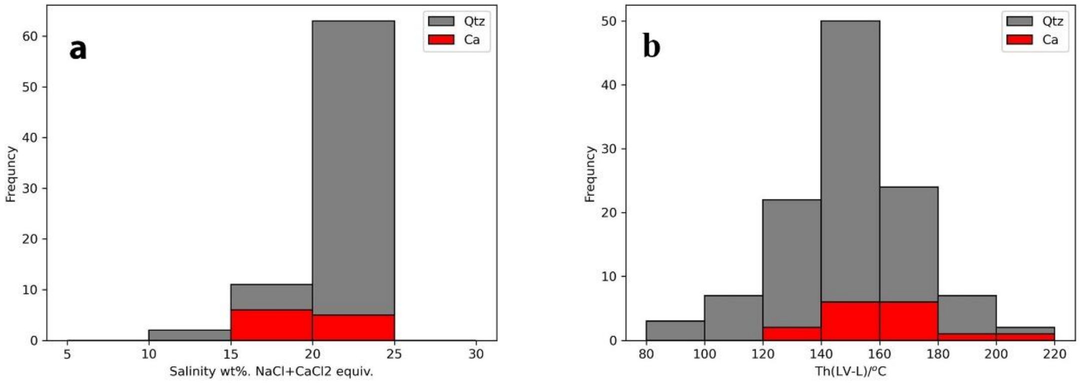

Figure 15

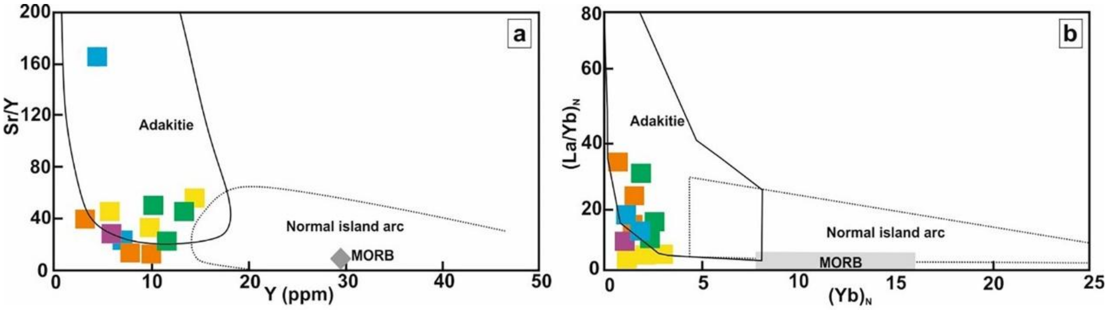

Figure 16

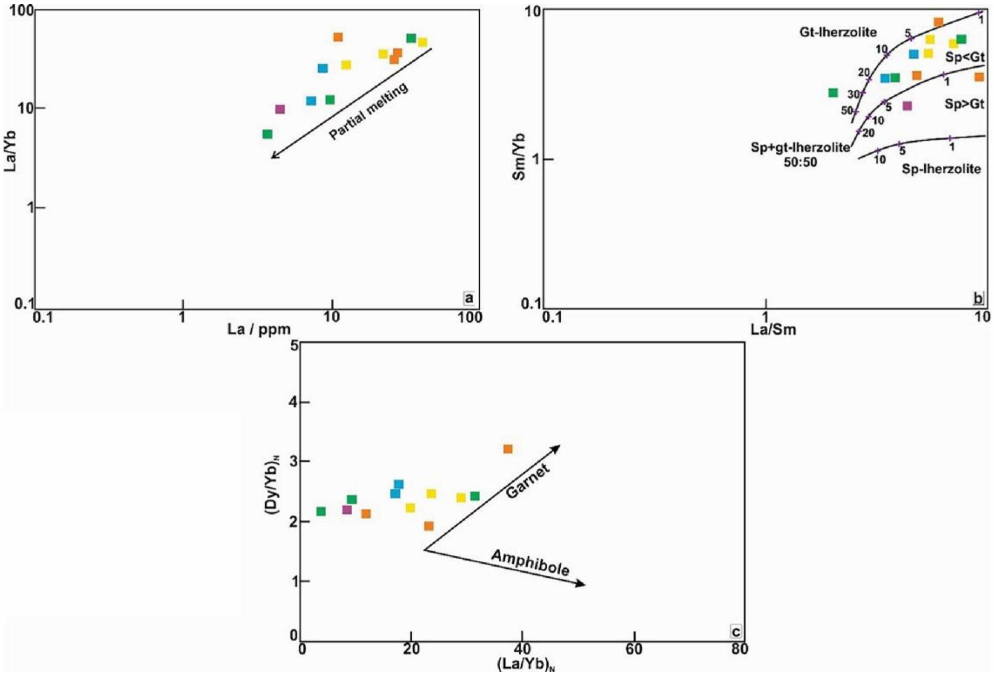
La/Yb
La / ppm
Partial melting
a
Sm/Yb
La/Sm
Gt-lherzolite
Sp<Gt
Sp>Gt
Sp+gt-lherzolite
50:50
Sp-lherzolite
b
(Dy/Yb)$_N$
(La/Yb)$_N$
Garnet
Amphibole
c

Figure 17

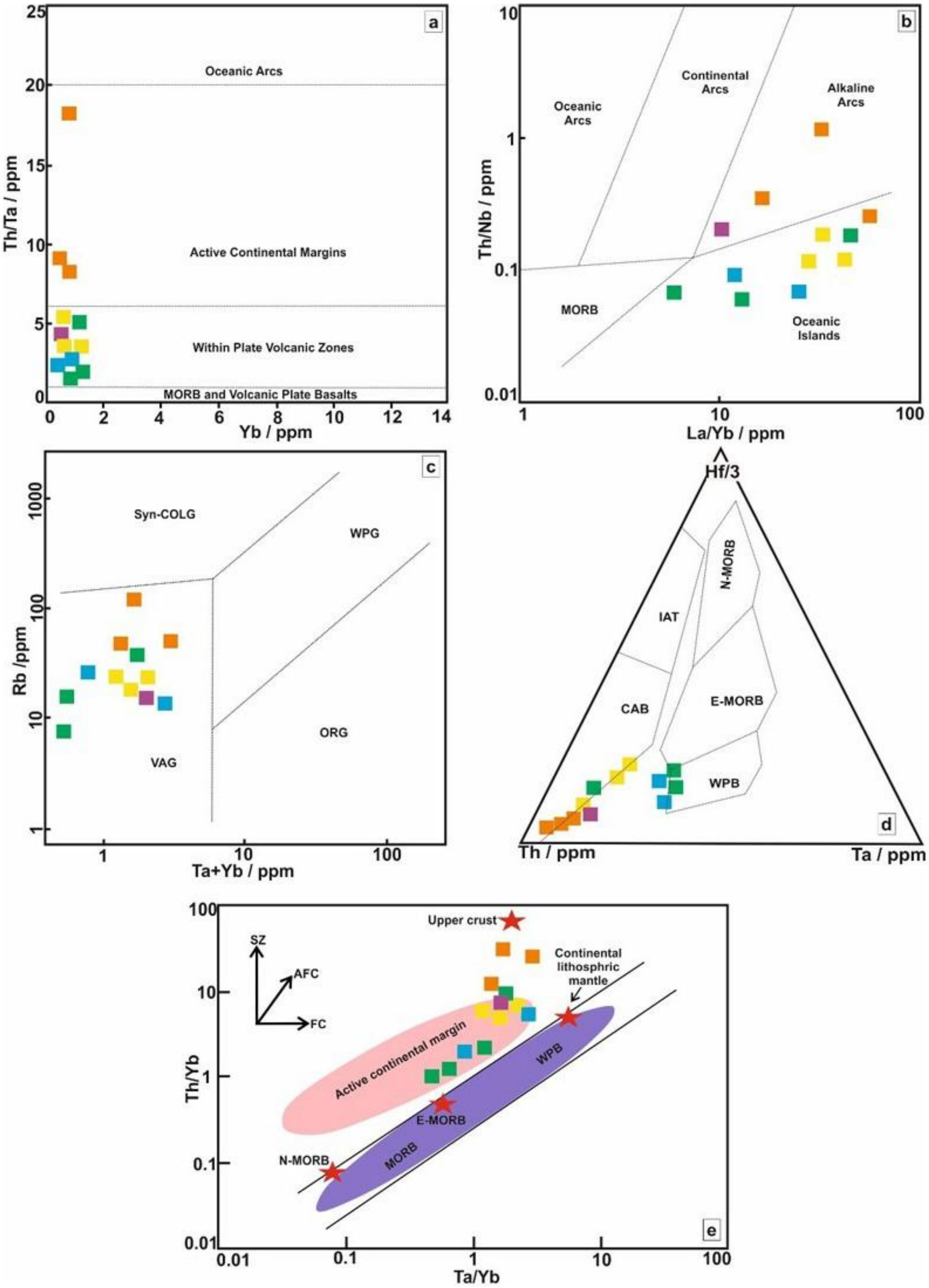

Figure 18

https://doi.org/10.5281/zenodo.15130089

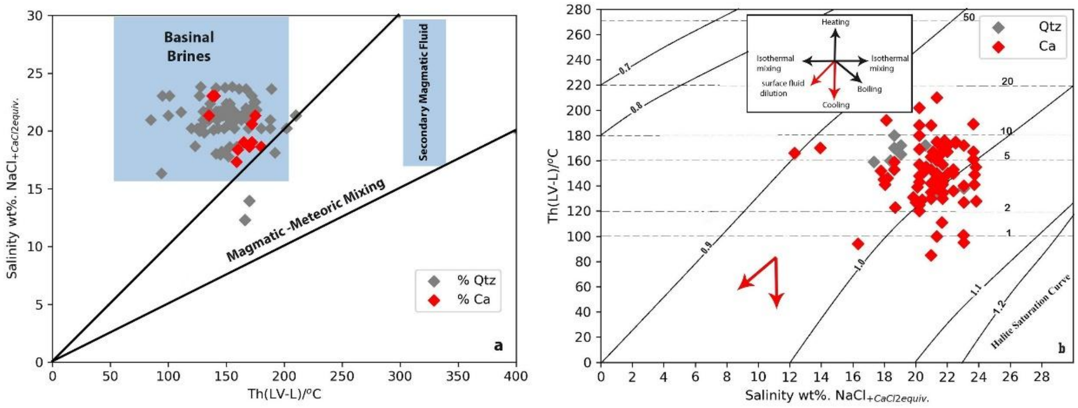

Figure 19

Appendix Table 1. X-ray diffraction (XRD) data.

Sample	Major phase	Minor phase
FA46	Albite+ Quartz	Calcite+ Illite+ Muscovite
FA008	Quartz+Albite+ Calcite	Muscovite+ Illite
FA11	Quartz+Albite+ Muscovite	Orthoclase
FA007	Quartz+Orthoclase+Albite+ Muscovite	–
FA051	Quartz+Calcite+Albite+ Orthoclase	Muscovite
FA049	Orthoclase+Quartz+Calcite+Albite+ Magnetit+Muscovite	–
FA066	Orthoclase+ Quartz+ Albite	Illite+ Muscovite
FA060	Albite+ Quartz	Montmorillonite-Cholorite

Appendix Table 2. Major, trace, and REE elements analysis of least–altered volcanic rocks from the Fathabad deposit.

		FA012	FA011	FA010	FA009	FA008	FA007	FA006	FA005	FA004	FA003	FA002	FA001
	Detection Limit	Basaltic-trachyandesite			Trachybasalt			Trachyandesite		Trachyte, Trachydacite	Rhyolite		
SiO_2 (wt.%)		50	49	51	50	47	51	55	58	67	69	72	74
Al_2O_3		15	19	16	14	18	17	19	17	15	15	14	13
CaO		9.4	7.8	7.8	8.5	6.3	7.8	4	3	2.9	1.8	1.2	0.9
MgO		2.2	1.1	5.1	7.3	4.2	6.1	2	1.7	1.3	0.4	0.2	0.2
TiO_2		1	0.6	1.2	1	0.8	0.9	0.7	0.8	0.4	0.8	0.8	0.8
Fe_2O_3		7.9	6.4	9.2	9.3	9.7	5.2	6.2	7.3	3.5	2.4	1.6	1.5
MnO		0.2	0.2	0.8	0.8	0.2	0.8	0.8	0.8	0.8	0.8	0.8	0.8
P_2O_5		0.8	0.5	1.1	0.9	0.4	0.4	0.6	0.5	0.2	0.3	0.1	0.1
Na_2O		3.6	2.8	3.3	3	4.1	5	3.8	4.4	3.5	3.8	3.3	3.4
K_2O		3.9	5.5	3	2.9	1.5	0.7	5.7	3.5	5.1	5.6	5.7	5.9
L.O.I		6	6.3	1.8	2.4	7.4	5.6	2	3.4	0.9	1.4	1.2	0.9
TOTAL		99	100	100	100	100	100	100	101	101	101	101	101
La	1 ppm	22	12	38	37	9.8	3.9	8.5	7	4.5	11	10	23
Ce	0.5 ppm	46	27	74	70	24	12	19	20	10	24	23	40
Pr	0.05 ppm	5.2	3	8.2	7.6	2.7	1.4	2.2	2.2	1.2	2.8	2.7	4.5
Nd	0.5 ppm	20	11	31	28	11	6.5	8.5	9.2	4.4	9.9	9.7	14

https://doi.org/10.5281/zenodo.15130089

Sm	0.02 ppm	4	2.3	5.4	5	2.7	2	1.9	2.1	1	1.9	2.2	2.5
Eu	0.1 ppm	1.6	0.7	1.2	1.2	0.9	0.7	0.5	0.5	0.2	0.3	0.2	0.2
Gd	0.05 ppm	3.3	2	4.5	4.3	2.8	2.2	1.6	2.1	1.1	1.5	2	2.2
Tb	0.1 ppm	0.4	0.3	0.6	0.6	0.4	0.4	0.2	0.3	0.2	0.2	0.3	0.3
Dy	0.02 ppm	2.4	1.5	3.3	3.1	2.7	2.3	1.3	2	1.2	1	2	2.1
Ho		0.5	0.3	0.6	0.6	0.5	0.5	0.2	0.4	0.3	0.2	0.4	0.4
Er	0.05 ppm	0.7	0.4	1	1	0.8	0.7	0.4	0.6	0.4	0.3	0.6	0.6
Tm	0.1 ppm	0.2	0.1	0.2	0.2	0.2	0.2	0.1	0.2	0.1	0.1	0.2	0.2
Yb	0.05 ppm	0.7	0.4	0.9	0.9	0.8	0.7	0.3	0.6	0.5	0.2	0.6	0.7
Y	0.5 ppm	9.8	5.5	15	14	11	10	4.4	6.9	5.2	3	7.3	9.9
Hf	0.5 ppm	0.8	1.9	2.5	3.1	0.8	0.9	1	1	0.3	0.2	0.3	0.5
Th	0.1 ppm	4.4	3.1	5.4	7.5	1	0.7	2.1	1.2	3.5	5.6	7.4	22
Ta	0.1 ppm	0.8	0.9	1.6	1.4	0.5	0.4	0.9	0.6	0.8	0.6	0.9	1.2
Ga		11	15	17	16	16	12	15	16	11	12	13	12
Cs	0.5 ppm	0.5	2.2	0.5	0.6	1.2	0.6	0.8	0.6	3.5	2.1	1.3	2.2
Cr	1 ppm	103	63	116	156	67	67	65	62	66	81	87	63
Li	1 ppm	16	5.9	11	16	21	27	14	15	22	5	5.7	5.6
Be	0.2 ppm	0.6	1.5	1.8	1.5	0.8	1.3	1.5	0.7	0.7	0.5	1	1.6
Nb	1 ppm	24	29	48	44	14	10	30	15	17	20	21	19
Rb	1 ppm	23	22	17	38	14	8.2	12	26	20	46	45	110
Sr	1 ppm	265	218	627	557	137	466	704	145	132	94	67	45
Zr	5 ppm	38	81	135	185	20	50	45	34	6.8	5.8	9.6	14
Ba	1 ppm	556	469	537	454	33	116	714	346	268	332	196	85
Sn	0.1 ppm	6.4	3.7	4.4	7.3	1.8	1.7	2.2	2.3	18	4	5.6	13
Co	1 ppm	13	9	25	26	16	18	12	7.6	7.2	2.3	2.4	2.1
Sc	0.5 ppm	6.5	2.3	11	11	10	13	2.1	3.3	2.3	0.8	2.4	1.3
W	1 ppm	1.8	1.2	1.5	2.2	2.1	0.8	1.2	4.5	2.4	1.7	0.9	1.9
V	1 ppm	125	72	145	148	167	156	88	38	43	10	6.3	6
U	0.1 ppm	1.1	1.1	1.2	1.8	0.3	0.3	0.8	0.3	2.4	1.9	1.8	3.3
Ni	1 ppm	35	11	45	85	8	48	11	5.7	8.4	7.1	7.1	7.6
Mn	5 ppm	1196	925	1009	887	826	714	293	431	444	522	90	136
Pb	1 ppm	84	29	16	170	16	17	26	16	41	55	62	91
Zn	1 ppm	307	64	126	105	68	185	72	74	86	107	63	88
Mo	0.1 ppm	1	2.8	3.4	1.2	0.9	1.2	1.6	1	2	2.3	1.8	1.8
Cu	1 ppm	1258	281	4.7	679	1	3.5	4.8	4.4	66	42	19	29
As (ppm)	0.1 ppm	6.4	5.5	6.9	7.3	6.2	6.1	7.6	6.4	7	6	19	5.9
Au (ppb)		190	199	187	15.25	580	251	678	617	10	-	3021	1313
Sr/Y		27	39	43	40	13	45	161	21	25	31	9.1	4.5
Eu/Eu_N		1.4	0.97	0.74	0.77	0.97	1.06	0.95	0.77	0.61	0.51	0.28	0.19
$(La/Yb)_N$		23.7	20	29.4	31.2	8.75	3.99	17.8	8.36	7.02	37.6	11.9	23.3
$(Dy/Yb)_N$		2.48	2.2	2.4	2.4	2.24	2.16	2.56	2.19	1.73	3.19	2.11	1.92
$(Sm/Yb)_N$		6.8	5.73	6.45	6.56	3.68	3.2	6.04	3.83	2.51	9.99	3.79	3.92

Appendix Table 3. Summary of microthermometric data from the primary Two-phase (LH2O+vapour) FIs of the quartz and calcite minerals from the Fathabad Cu±Au deposit.

Notes 1. Te (Ice): eutectic temperature; Tm(Ice): final ice melting temperature; Th: homogenization temperature. The salinities of H_2O- $NaCl+CaCl_2$ systems were calculated using the ice points (Tm(ice); after Bodnar (1993). Density in the H_2O-$NaCl+Cacl_2$ system after Flincor software Brown (1989).

Host mineral	FI Number	Size (µm)	Type	Origin	Te / °C	Tm(ice) / °C	Salinity wt% NaCl+CaCl2	Th (°C) Min/Ave/Max	Density /g/cm3
Quartz	115	4 to 35	LV	Primary	−41 to −52	−8.4 to −24.7	12.30 to 23.83	85/150/ 210	0.99 to 1.16
Calcite	16	4 to 12	LV	Primary	−41 to −52	−14 to −21	17.33 to 23.05	135/160/208	1.03 to 1.10

Appendix Table 4. Fathabad gold copper deposits and some epithermal deposits in Iran.

Main feature	Fathabad Deposite	Khalifehlu deposit	Goluje epithermal deposit	cheshmeh Noghreh
Base metals	Cu- Au	Cu- Au	Base metals	Cu- Au
geographical location	Fathabad-Roshtkhar	Tarom,North of Khoramdareh	North of Zanjan	Southwest of Kashmar
structural zone	Khaf- Dorouneh	Tarom magmatic zone	Tarom–Hashtjin	Khaf- Dorouneh
Host Rock	andesite, latite-andesite amygdaloidal and granite	lava and pyroclastic quartz monzonite porphyry	basaltic andesite, andesite and trachy andesite, dacite and tuff	pyroclastic
age of mineralization	Eocene	Eocene	Eocene- Oligocene	Tertiary
Control of mineralization	Joint, fracture, fault	fault	Joint, fracture, fault	fault
Mineralogy	chalcopyrite, galena, pyrite, burnite, covelite	chalcopyrite, bornite, gold, pyrite, Covelite	galena, sphalerite, chalcopyrite and pyrite	pyrite, iron oxides, malachite and azurite
texture and structure	Massive, stripe,Radial, comb, vein-veinlet, shear, scatterd, carbonate substituted	vein-veinlet, Shear, vesicular, massive	Shear, stripe, veinlet, dispersed distribution of mineral grains	dispersed distribution of mineral grains, voids filling, vein-veinlet
Alteration	Quartz, chlorite, epidote, Carbonate and sericite	Quartz, alunite	arjelic, phyllic, and propylitic, silicic	arjelic, propylitic, sericite
type of Mineralization	Epithermal (LS)	Epithermal (HS)	Epithermal (LS)	Epithermal (LS)
Reference	This paper	HOSSEINZADEH et al. (2015)	MEHRABI et al. (2009)	ALAMINIA et al. (2010)

Appendix Table 5. Sulfur isotope values of chalcopyrite in quartz vein.

Sample name	Rock	Sulphide mineral	Quartz vein	δ^{34}S(‰)	δ^{34}SH_2S
BHFA-B35	Porphyritic andesite	Chalchopyrite	Quartz+ Chalchopyrite+pyrite+malachite+Hematite	-1.58	-1.94
BHFA-B12	Porphyritic andesite	Chalchopyrite	Quartz+ Chalchopyrite+pyrite+Chalcocite+malachite+Hematite	-2.86	-3.15

https://doi.org/10.5281/zenodo.15130089